Editors' Suggestion

Modal analysis with proper orthogonal decomposition of hypersonic separated flows over a double wedge

Ozgur Tumuklu* and Deborah A. Levin†
University of Illinois at Urbana-Champaign, Urbana, Illinois 61801, USA

Vassilis Theofilis‡
University of Liverpool, Liverpool L69 3GH, United Kingdom

(Received 3 August 2018; published 19 March 2019)

The unsteady behavior of an Edney type-IV shock-dominated hypersonic separated flows over a double-wedge geometry for different gas compositions are studied using the time-accurate direct-simulation Monte Carlo (DSMC) and window proper orthogonal decomposition (WPOD) methods. Near steady state, we find that the POD modes can be correlated with the global modes predicted by linear stability theory. The WPOD analyses show that the first mode for each flow quantity outlines the corresponding steady-state solution and that higher spatial POD modes are pronounced in the bow shock, separation, and transmitted shocks and shear layers, thereby coupling these regions. The temporal modes corresponding to each macroscopic flow quantities are observed to have the same decay rates. The effects of three types of gas compositions—molecular nitrogen, nonreacting air consisting of molecular nitrogen and oxygen, and reacting air with oxygen dissociation and the $N_2 + O$ exchange reactions—on flow stability are considered. Nonequilibrium thermochemical effects are found to change the shock structures, the size of the separation region, and the time required to reach steady state. The decay rate of the least damped eigenmode for the chemically reacting air case is found to be smaller in comparison to the nonreacting air case since the translational temperatures downstream of the bow shock are lower due to endothermic chemical reactions. The simulated heat fluxes and shock standoff distance are found to be in qualitative agreement with recent experiments where the freestream density is eight times higher than the current DSMC computations.

DOI: 10.1103/PhysRevFluids.4.033403

I. INTRODUCTION

Hypersonic shock-wave laminar boundary-layer interactions (SWBLIs) are characterized by a wide range of temporal and spatial variations with distinct degrees of thermochemical nonequilibrium. Accurate modeling of SWBLIs is crucial for design purposes of hypersonic vehicles in order to avoid performance penalties. Experimental studies on separated hypersonic flows on hollow cylinder/flare and biconic configurations were conducted by Holden and Wadhams [1] in shock tunnels at Calspan–University of Buffalo Research Center (CUBRC) for code-validation purposes, and Navier-Stokes solutions (NS) [2] were found to be in good agreement with the experiments for high densities and low stagnation enthalpies where thermochemical nonequilibrium effects and boundary layer slip are not important [3]. Further experiments on double-cone and wedge configurations were recently performed by Swantek and Austin [4] and the impact of the thermochemical state

*tumuklu2@illinois.edu
†deblevin@illinois.edu
‡v.theofilis@liverpool.ac.uk

of the gas on SWBLIs by changing the chemical composition from nitrogen to air for stagnation enthalpies from 2 to 8 MJ/kg were investigated. However, discrepancies between the calculated and measured heat fluxes were observed, especially for high stagnation enthalpies [5]. In addition, previous experimental and numerical studies [6–8] showed that shock/turbulent boundary-layer interactions cause unsteady shock motions related to both upstream and downstream conditions. However, characterization of the time-dependent behavior of SWBLIs in ground-based facilities can create additional challenges due to limited measurement times and the lack of a well-established metric to relate the establishment time in short-duration facilities [9]. Therefore, the effects of thermochemical nonequilibrium on SWBLIs in the hypersonic regime are still under investigation.

In our previous work [10], considerable unsteadiness was observed in the bow and separation shocks, and shear layers for hypersonic shock-dominated nitrogen flows over a double cone. The unsteady characteristics of SWBLIs were accurately modeled using the inherently time-accurate direct simulation Monte Carlo (DSMC) method and the residuals algorithm of Theofilis [11]. The unsteady DSMC signal at critical locations such as the separation point, shock location, and shear layers was postprocessed to obtain the features of the least damped eigenmode. It was observed that increasing the Reynolds number resulted in a decrease in the magnitude of the damping rate, which, in turn, increased the required time to reach steady state. Further analyses revealed that the bow shock oscillations and a Kelvin Helmholtz instability become dominant for the highest unit Reynolds number of 374 000 m^{-1} considered in our study. We used a similar approach in Ref. [12] to investigate the time characteristics of massively separated hypersonic flows with different leading edge configurations of a "tick" shape geometry based on the unsteady DSMC signal at the previously determined critical locations. The objective of this work is to investigate the impact of internal relaxation and chemical reactions on the time characteristics of a Mach $\sim$7 unsteady flow over a 30/55-deg double wedge similar to the conditions measured by Swantek and Austin [4]. As for the double cone, the double wedge also exhibits Edney IV interactions [13].

Under certain conditions, thermochemical nonequilibrium potentially alters shock structures, surface parameters, and the stability characteristics of SWBLIs. The effects of high-enthalpy thermochemistry on Edney IV interaction [13] were investigated and a coherent unsteadiness at the jet impingement location was observed in the experiments of Sanderson *et al.* [14]. The shock oscillations were attributed to shedding vortices generated by the jet and blunt body interactions based on the numerical simulations of Furumoto *et al.* [15]. Furthermore, due to endothermic chemical reactions, the peak surface flux and pressure values of Ref. [15] decreased when thermochemical nonequilibrium was included, as opposed to the simulations of Ref. [16] in which the surface heat flux increased significantly due to recombination reactions at the wall. The effects of high temperatures on the stability of hypersonic boundary layers assuming thermal and chemical equilibrium were also studied by Malik *et al.* [17], but thermochemical effects could only be modeled in the mean flow and not directly in the stability equations since the inclusion of such effects made the system stability equations intractable. It was observed that chemical reactions made the first mode more stable, whereas it destabilized the second mode [17]. For flows that have a much greater range of length scales, such as considered in the work presented here, boundary layer transitions would not be the main mechanism for unsteadiness. Therefore, thermochemical nonequilibrium, the extent of the separation zone, and viscous-inviscid interactions will determine the general stability characteristics of hypersonic separated flows.

In this work, the DSMC method [18], a well-known particle-based stochastic approach for solving the Boltzmann equation of transport, is applied to hypersonic separated flows over a double-wedge configuration for multiple, reacting species since it provides the highest fidelity of molecular thermal nonequilibrium phenomena, an accurate model of transport properties, and inherently captures velocity and temperature slip, as opposed to conventional NS solutions where an *a priori* model is required to model the velocity slip and temperature jump. Figure 1 shows the complex SWBLIs and time-dependent flow features captured by DSMC that will be discussed further in Sec. II for three chemical systems. To specifically quantify the unsteadiness in those regions of the flow that theory and previous simulations indicate strongly effect the global time

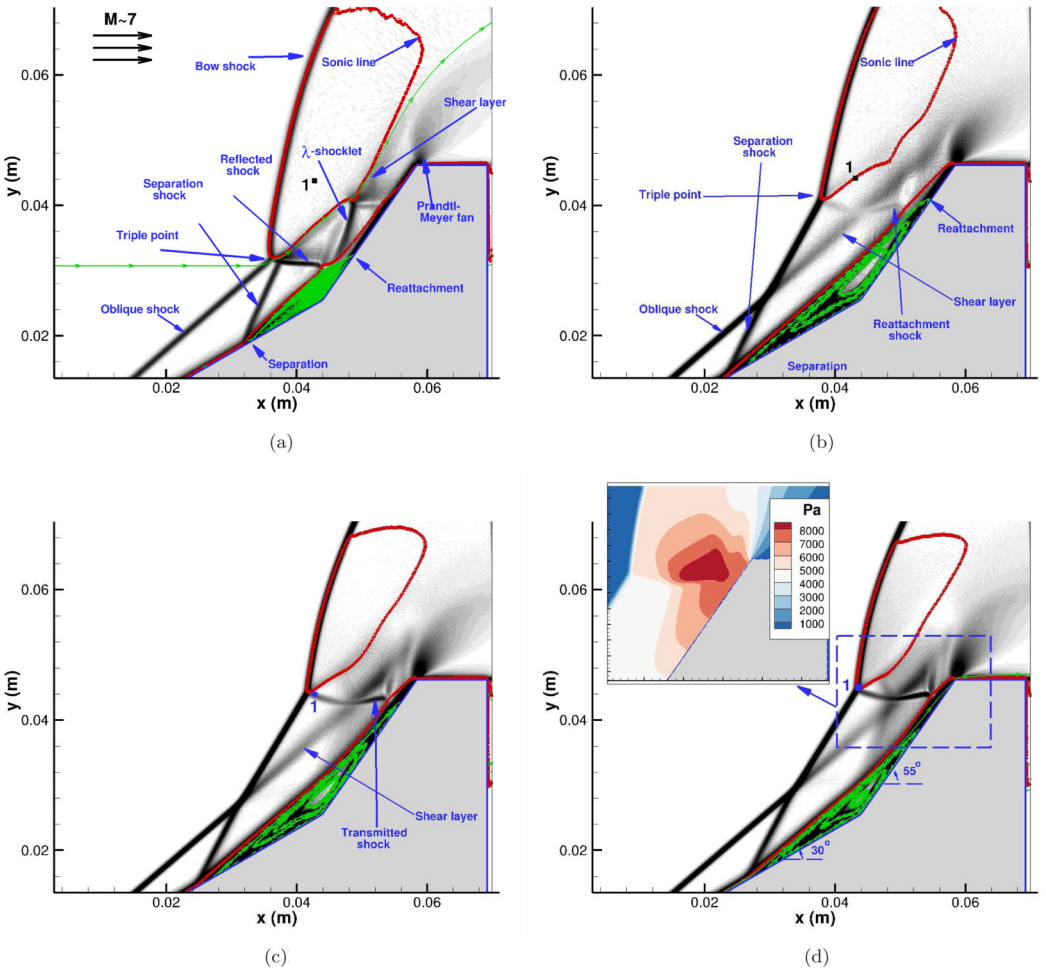

FIG. 1. Transient shock structure prior to steady state, except for (b), for different gas species based on computed schlieren of this work. The inset shows the spatial distribution of the pressure values in the vicinity of the second cone surface. See Sec. IV D for estimates of times to reach steady state. See also the Supplemental Material in Ref. [20] for the time evolution of the flow-field parameters. (a) Nitrogen at 0.1 ms, (b) Nitrogen at steady-state, (c) Non-reacting air case at 1.275 ms, and (d) Reacting air case at 2 ms.

evolution, we specifically placed "numerical" probes at selected locations since the data storage for the entire flowfield at each time step would have been prohibitive. Figure 2 shows one such location, the triple point, where it can be seen that there are dramatic changes in the time dependency of macroparameters such as temperature, velocities, and pressure for the same free-stream conditions but different chemical compositions. Because these flows are unsteady, however, and since they do not exhibit the simple exponential decay that we observed in our earlier nonreacting nitrogen flows over a double cone [10], the determination of the locations where numerical probes should be placed would require a prerun simulation and a large amount of trial and error. The second objective of this work is to apply a proper orthogonal decomposition (POD) [19] technique to extract time characteristics of DSMC particle data throughout the entire flow field.

When one wants to understand the coupling of different regions of the flow as it evolves, the two general choices are to formulate the stability equations as in the case of operator-based approaches consistent with kinetic methods or to employ data-driven methods such as proper

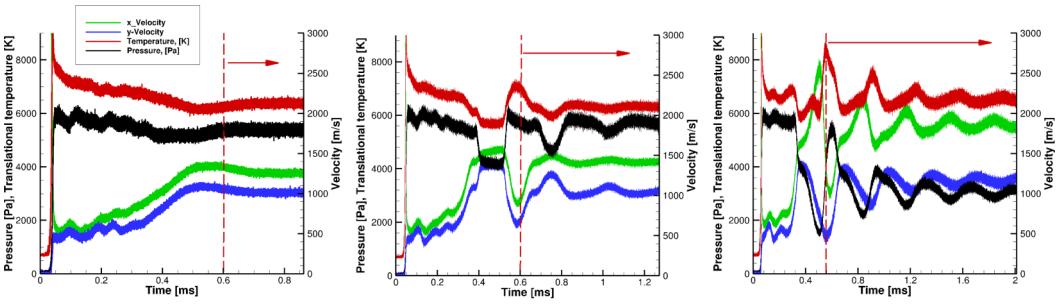

FIG. 2. Time variation of flow-field parameters in the vicinity of the triple point (see location 1 in Fig. 1). Red arrows indicate the time intervals where the WPOD algorithm will be applied. (a) Nitrogen, (b) Non-reacting air, and (c) Reacting air.

orthogonal decomposition (POD) [19] and dynamic mode decomposition (DMD) [21]. The proper orthogonal decomposition (POD) method [19] has been used to reduce large amounts of multidimensional data to low-dimensional approximation descriptions based on orthonormality, ensuring that main features of the actual data are preserved. DMD provides insights about dynamics by decomposing data into the spatiotemporal parts for diagnostics, prediction of future states, and control purposes [22,23]. As opposed to POD, where frequencies of modes can be mixed, resulting in a complicated physical interpretation, the DMD method identifies a growth and decay rate and a characteristic frequency corresponding to each mode [24]. Nonetheless, the POD method is the most commonly used technique in the fluid mechanics community to extract coherent structures of turbulent flows due to its simplicity [25,26]. As will be discussed in Sec. III, the window proper orthogonal decomposition (WPOD) is a more efficient approach in comparison to the POD method. Therefore, we adopted the WPOD method in this work since it is a commonly used approach to diminish statistical fluctuations and to analyze the time characteristics of flows. For example, Grinberg [27] recently applied the WPOD method to the particle-based simulation technique of molecular dynamics to increase the quality of the numerical simulations by eliminating statistical fluctuations from the ensemble average.

The outline of the remainder article is organized as follows. In the next section, we describe the flow conditions, the general features of the unsteady SWBLIs, and their effect on surface parameters including heat flux, which is often measured in ground-based facilities. In Sec. III, we provide a brief overview of the window proper orthogonal decomposition technique that we will use to investigate the impact of internal relaxation and chemical reactions on the time characteristics of the flow. To the best of our knowledge, this is the first time the WPOD method is used to decouple time variations into the spatiotemporal modes with the intent of understanding thermochemical effects. We will use WPOD to correlate the POD modes with global modes, to eliminate statistical fluctuations from unsteady DSMC signal, and to predict future states without running computationally demanding DSMC simulations for long periods of time. Section IV is devoted to examining the time dependencies of the different gas cases, providing a comparison about the number of active modes, how they decay in time, and how they correlate with the global modes obtained using the residuals algorithm of Theofilis [11,28]. The appendices provide details regarding the DSMC model in terms of models and numerical parameters, numerical convergence of POD parameters, and a summary of WPOD parameter fit results.

II. TEMPORAL CHANGE OF SHOCK STRUCTURES AND SURFACE FLUXES

We consider the Mach 7 flow over a 30/55-deg double-wedge configuration studied in the experiments of Swantek and Austin [4] in their high-expansion-tube (HET) facility for chemical

TABLE I. Free-stream conditions for different cases.

Freestream parameter[a]	Value
Mach number	7.14
Temperatures,[b] K	710
Static pressure, Pa	98
Velocity, u_∞, m/s	3812
Number density, molec/m^3	1.0×10^{22}
Stagnation enthalpy, MJ/kg	8.0
Unit Reynolds number, 1/m	5.22×10^{4}
Mean free path, m	1.64×10^{-4}
Knudsen number	3.24×10^{-3}

[a]The mass fraction of air is 79% N_2 and 21% O_2 for both reacting and nonreacting cases.
[b]In thermal equilibrium ($T_{\rm trn} = T_{\rm rot}$=$T_{\rm vib}$).

compositions of nitrogen and air and an enthalpy of 8 MJ/kg. The free-stream conditions used in the current work are presented in Table I, where the free-stream number density is decreased by a factor of about eight in comparison to the experiment. These simulations will be referred to "density-degraded cases" since our previous work revealed that the experimental case did not reach steady state for both two- and three-dimensional (2-D and 3-D) geometric configurations [29,30] for the experimental runtime of 0.242 ms. Therefore, this lower density case, also recently modeled for the running gas of nitrogen with a 3-D model by Sawant *et al.* [31], is the target problem to reduce the DSMC computational cost using a 2-D model and to ensure that the flow reaches steady state for three different cases. For the *nitrogen* case, elastic and inelastic internal relaxation reactions were modeled. Since the stagnation enthalpy of 8 MJ/kg is relatively low, the dissociation reactions of nitrogen are negligible and not modeled in the current work. On the other hand, due to the lower bond energy of oxygen molecules in comparison to that of nitrogen, the dissociation reaction of oxygen given in Eq. (1) is modeled along with the exchange reactions of O atoms with N_2 molecules,

$$M + O_2 \rightarrow M + O + O, \tag{1}$$

$$N_2 + O \rightarrow NO + N, \tag{2}$$

where M stands for N_2 or O_2 and it is assumed that the reverse reactions are not important. A separate study showed that the oxygen dissociation rate is five orders of magnitude higher than the reverse recombination rate and that the molecular dissociation rate is two orders of magnitude less than that of molecular oxygen dissociation. Therefore, recombination rates involving atomic oxygen and nitrogen species do not have any impact on the flow and are neglected. This configuration is known as the *reacting air* case. In order to see the effect of the chemical reactions on the flow-field parameters more closely, these chemical reactions were deactivated and only molecular elastic and inelastic collisions between molecules were allowed to quantify the effect of molecular transport and thermochemical nonequilibrium. This configuration is called *nonreacting air* case.

With these conditions, the principal shock-shock interaction features for different gases obtained in the DSMC simulations are seen in the computed schlieren image shown in Fig. 1. Overall, the figure shows the oblique shock formed at the first wedge, which interacts with the detached bow shock generated by the second wedge. These outer shocks are further modified by a strong separation zone resulting from large adverse pressure gradients and the associated separation and reattachment shocks resulting in a time-dependent flow field with coupled features such as the triple point, shock impingement, boundary-layer interactions, and shear layers. Viscous forces are prominent at the shear layers formed in the vicinity of the separation region and between the

supersonic flow coming through the oblique shock and subsonic flow after the strong bow shock. The interaction of the oblique and bow shocks creates a transmitted shock which reflects between the second wedge surface and the shear layer, resulting in a λ-shocklet that shows a time-dependent behavior. A comparison of Figs. 1(a) with 1(b) reveals that the separation shock moves upstream due to an increase in the size of the separation zone for the nitrogen case. Therefore, the λ shocklet becomes more obscure in time due to the movement of the triple point. These coupled interactions also depend on gas species. As can be seen in Figs. 1(c) and 1(d), the triple point is found to be closer to the wedge shoulder for the nonreacting and reacting air cases. The size of the subsonic region after the bow shock is found to be similar for the nonreacting and reacting air cases but less in comparison to the nitrogen case which can be attributed to chemical reactions and molecular interactions between oxygen and nitrogen. As can be seen by comparing Figs. 1(d) with 1(b), the interaction of the transmitted shock with shear layer results in a larger gradient and pressure values for the reacting air case. It should be noted that results shown in Figs. 1 and 3 for the given times represent an average over 500 time-step samples collected before and after the indicated times. This sample size is large enough to reduce the statistical noise but is sufficiently small to capture the unsteadiness since a small time step of 3 ns is used for all cases.

The time evolution of the shock structure has significant impacts on the surface parameters as well. As can be seen in Fig. 3(a), the heat fluxes at around $x = 0.03$ m decrease in time due to the increase of the separation zone for the nitrogen case. The maxima shifts in the downstream direction with a decrease in its magnitude associated with a weaker shock interaction. A similar trend can be seen in Fig. 3(b) for the reacting air case. Note that there is a sudden decrease at around $x = 0.049$ m at 0.075 ms, as opposed to the nitrogen case where the heat fluxes almost monotonically increase along the second wedge surface until the maximum value. This can be attributed to the differences in the size of the separation region. More specifically, for the nitrogen case, a larger separation zone prevents the transmitted shock from interacting with the boundary layer of the second wedge. Therefore, there is no trace of the transmitted shock on the heat fluxes for the nitrogen case. Note that, as will be discussed in the next section, although the time characteristics of the nitrogen and reacting air cases are different, a comparison at 0.1 ms indicates that the maximum heat transfer rate for the reacting air case is somewhat larger than that for the nitrogen case. This is due to the fact that the interaction of the transmitted shock with the boundary layer results in a larger gradient which increases the maximum value, as shown in Fig. 3(c) with the solid green line. A similar trend was seen in the experiments of Swantek and Austin [4] even though the density of the air and pure nitrogen experiments is larger by a factor of eight compared to the current DSMC calculations. Nonetheless, the measured and calculated heat fluxes are found to be qualitatively similar and scale in magnitude. In particular, the aforementioned trend at about $x = 0.05$ m occurs in the experiments as well. Also, the measured maximum value for the air case is higher than that of the nitrogen case. It should be noted that the current calculations do not model surface catalytic reactions because there are relatively few dissociation events. In fact, a comparison of a catalytic versus as noncatalytic simulation for the reacting air case only shows an increase of about 10% in the peak of the heat flux at $x = 0.055$ m, as can be seen in Fig. 3(d). However, catalytic reactions can further increase the surface heating rates at higher stagnation enthalpies, as discussed in Ref. [16].

However, the difference between the maximum of heat fluxes for the nitrogen and nonreacting cases decreases close to steady state, as can be seen in Fig. 3(d). In fact, the small difference of 15% can be attributed to the endothermic dissociation and exchange reactions removing energy from the flow, which in turn results in a decrease of the maximum value for the reacting air case. Lastly, a comparison of the slip velocities for different gas species is shown in Fig. 3(e). The DSMC method inherently captures velocity slip with the Maxwell gas-surface interaction model without an *a priori* model, as opposed to CFD approaches. Since Knudsen numbers for these cases are essentially the same, the slip values are also found to be the same for all locations and at the separation point where the velocity slip becomes zero. In particular, close to steady-state, calculations based on the axial distance difference between the locations where slip values become zero predict the size of separation regions for the nitrogen, nonreacting air, and reacting air cases are 0.030, 0.029, and

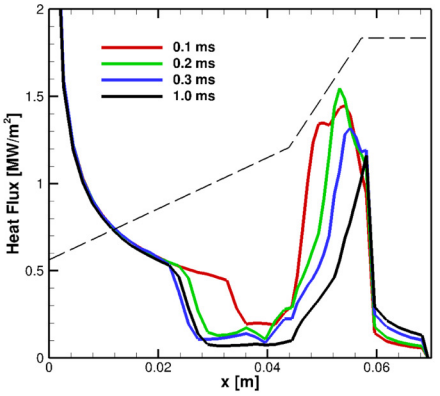

(a)Heat fluxes for nitrogen in time

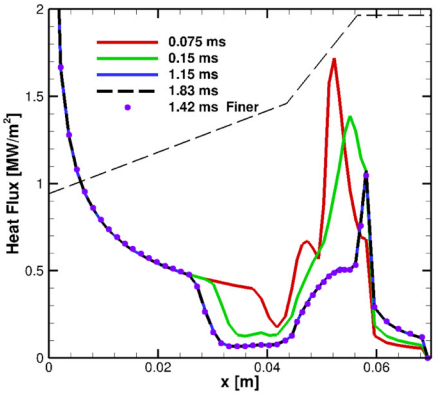

(b)Heat fluxes for reacting air in time

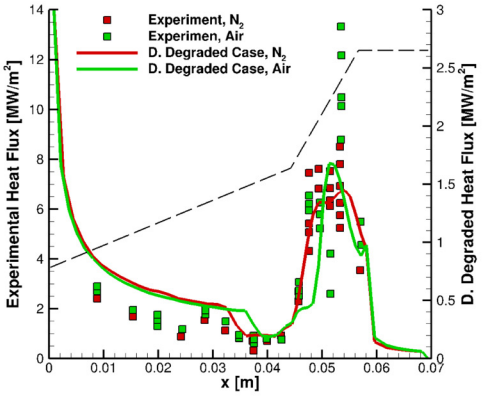

(c)Comparison of heat fluxes for the experiment [31] and the density degraded cases at 0.1 ms

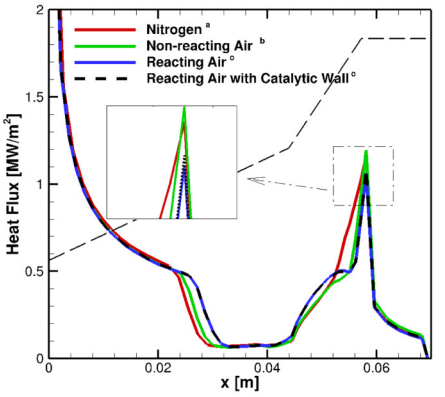

(d)Heat flux comparison for different gases and the effect of surface catalycity for the reacting air case

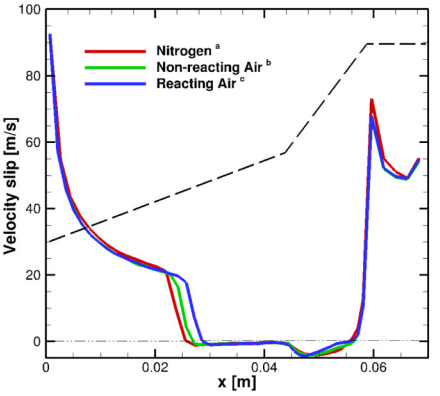

(e)Velocity slip

FIG. 3. Variation of surface parameters with different gas species in (d) superscripts *a* at steady state, *b* at 1.275 ms, and *c* at 2 ms. Note different *y* scales in (c) where the left axis of panel (c) corresponds to the experimental surface heat flux whereas the right axis corresponds to the density-degraded case with eight times lower density compared to the experiments.

TABLE II. Constants for the evaluation of cross-sectional and rotational and vibrational constants.[a]

Species	Diameters d_{ref} [Å]	Viscosity index, ω	$Z_{r,\infty}$	T^* [K]	θ [K]	Viscosity coefficient [Nsm^{-2}]
N_2	3.58	0.68	15.70	80	3371	4.075×10^{-5}
O_2	3.37	0.68	14.40	90	2256	4.915×10^{-5}
NO	3.41	0.65	5	117	2719	4.525×10^{-5}
N	3.11	0.65				3.724×10^{-5}
O	2.96	0.65				4.391×10^{-5}

[a]At a reference temperature, $T_{\text{ref}} = 1000$ K.

0.027 m, respectively. The size of the separation region for the reacting air case is smallest due to the effects of the aforementioned chemical reactions. In particular, the decrease of the translational temperatures reduces the adverse pressure gradient. Therefore, the overall size of the separation region is smaller than the other cases. Similarly, the relatively smaller characteristic temperature of oxygen molecules (see Table II) results in larger vibrational temperatures after the bow shock for the nonreacting air case in comparison to the nitrogen case. This, in turn, reduces the overall translational temperatures for the nonreacting air case. Therefore, the size of the separation region is somewhat less in comparison to the nitrogen case. Our results are consistent with the continuum steady calculations of Ref. [15] that studied the effects of thermochemical nonequilibrium of SWBLIs for flows over a flat plate for an ideal vibrationally excited, but chemically frozen gas (i.e., similar to the nonreacting air case of the current work) and air-reacting cases. Finally, it was noted by Moss and Bird [32] that the selection of DSMC parameters is crucial to obtaining accurate heat fluxes for flows with small Knudsen numbers such as these. The DSMC numerical parameters used in this work (see Appendix A) were shown in our earlier work [10] of flows over a double cone to obtain convergence of heat flux values and agree well with experimental values.

To analyze the time dependency of SWBLIs more closely, the unsteady DSMC signal at critical locations was postprocessed to obtain the damping rate of the least damped global eigenmode, the amplitude function of the corresponding eigenmode, and the steady-state solution in our previous works [10,33,34]. As mentioned in the introduction, the DSMC signal at location 1 of Fig. 1 in the vicinity of the triple point for different gas species was monitored using numerical probes as was shown earlier in Fig. 2. For the nitrogen case, although high-frequency statistical fluctuations are still present, the flow seems to reach steady state after 0.7 ms, as can be seen in Fig 2(a). For the nonreacting air case, the sinusoidal fluctuations are observed after 0.7 ms, as can be seen in Fig. 2(b) and the flow does not reach steady state, although the flow conditions and the treatment of the chemical reactions are the same with the nitrogen case. For the reacting air case, these fluctuations shown in Fig. 2(c) become more prominent and the flow requires more time in order to damp these fluctuations out. See Ref. [20] for the movies showing the temporal evolution of the flow field parameters of three different gas species for details. In order to analyze this time dependency in a more accurate way with reducing statistical noise, the unsteady characteristics of the hypersonic separated flows will be investigated using the WPOD method.

III. WINDOW PROPER ORTHOGONAL DECOMPOSITION [27]

The POD method, introduced by Lumley [19], has been commonly used to extract dynamically important features of turbulent flows and can also reduce high-dimensional data to lower dimensional approximate solutions with the use of optimal sets of basis functions [23]. However, when the size of the data, n, is too large, the classical POD method produces an $n \times n$ intractable eigenvalue problem [23]. To reduce the computational burden, the method of snapshots [35] is an effective way of analyzing the temporal and spatial characteristics of the flow field based on different discrete snapshots. In particular, the method of snapshots reduces the problem to an $N_{\text{pod}} \times N_{\text{pod}}$ eigenvalue

problem, where N_{pod} is the number of time windows or snapshots and $N_{\text{pod}} \ll n$. Although the method of snapshots analyzes a smaller set of eigenvectors in comparison to the classical POD method, the eigenvalues and eigenvectors of both methods are closely related (see Ref. [23] for details). In this method, the F term is the stack form of a vector or a scalar field of the flow field parameters [23,36], $\mathbf{q}(x, y, t)$, and can be constructed based on discrete time windows. That is,

$$F(\tau, \boldsymbol{x}) = \begin{bmatrix} q_1^1 & q_1^2 & \cdots & q_1^{N_{\text{pod}}} \\ \vdots & \vdots & \vdots & \vdots \\ q_n^1 & q_n^2 & \cdots & q_n^{N_{\text{pod}}} \end{bmatrix}, \tag{3}$$

where $q = (u, v, T_{\text{trn}}, T_{\text{rot}}, T_{\text{vib}}, P, u_1, v_1, \ldots, u_2, v_2, \ldots)$ and subscripts 1 and 2 represent the different gas species modeled in this work (i.e., N, O, N_2, O_2, NO) and u, v, T_{trn}, T_{rot}, T_{vib}, and P are the x- and y-velocity field components, translation, rotational, and vibrational temperatures, and the pressure, respectively. The covariance matrix, C_{ij}, can be constructed with inner product of the F term. Namely,

$$C_{ij} = \int F(\tau^i, \boldsymbol{x}) F(\tau^j, \boldsymbol{x}) d\boldsymbol{x} = \boldsymbol{F}^T \boldsymbol{F} \in \mathbb{R}^{N_{\text{pod}} \times N_{\text{pod}}}, \tag{4}$$

where i and j correspond to the different number of snapshots (i.e., $i, j = 1, 2, 3, \ldots, N_{\text{pod}}$). Then, the kth temporal mode, $a_k(\tau)$, can be found by solving the eigenvalue problem of

$$\int C(\tau, \tau')\, a_k(\tau')\, d\tau' = \lambda_k\, a_k(\tau), \tag{5}$$

where $\lambda_1 \geqslant \cdots \geqslant \lambda_{N\text{pod}} \geqslant 0$. The spatial part of the kth mode, $\phi_k(x)$ can be computed based on the orthogonality relation. That is,

$$\phi_k(\boldsymbol{x}) = \int a_k(\tau)\, F(\tau, \boldsymbol{x})\, d\tau. \tag{6}$$

After decomposing spatial and temporal parts, unsteady data can be constructed as

$$\sum_{k=1}^{m} a_k(\tau) \phi_k(\boldsymbol{x}) = F(\tau, \boldsymbol{x}), \tag{7}$$

where m can be smaller than the number of snapshots (i.e., $m \leqslant N_{\text{pod}}$) and represents the number of dominant eigenmodes in the flow field, i.e.,

$$\sum_{j=1}^{N_{\text{pod}}} \lambda_j \approx \sum_{j=1}^{m} \lambda_j. \tag{8}$$

After decoupling the temporal and spatial parts of any macroscopic flow-field parameters, these POD modes can be used to predict future states. These unsteady flow characteristics close to steady state will be investigated closely in the next section. Note that the solution at steady state may be predicted by the first mode, ϕ_1.

The application of WPOD to the DSMC method is quite rare. In the work of Kumar *et al.* [37], WPOD was used to reduce the statistical noise in a DSMC simulation of a sonic jet expansion flow through a divergent nozzle for a steady-state flow. In DSMC, statistical fluctuations are inherent in the method because each computational particle represents on the order of 10^{13} true atoms or molecules. After sufficient collisions have occurred in a typical DSMC simulation, the flow has reached steady state, but the particle data is too noisy to provide meaningful macroparameters such as number density, temperature, velocities, etc. Therefore, collisions are continued, but sampling occurs, and since the statistics are assumed to be random, the magnitude of the fluctuations is inversely proportional to $\sqrt{N}$, where N is the number of samples. Since the flows that are considered

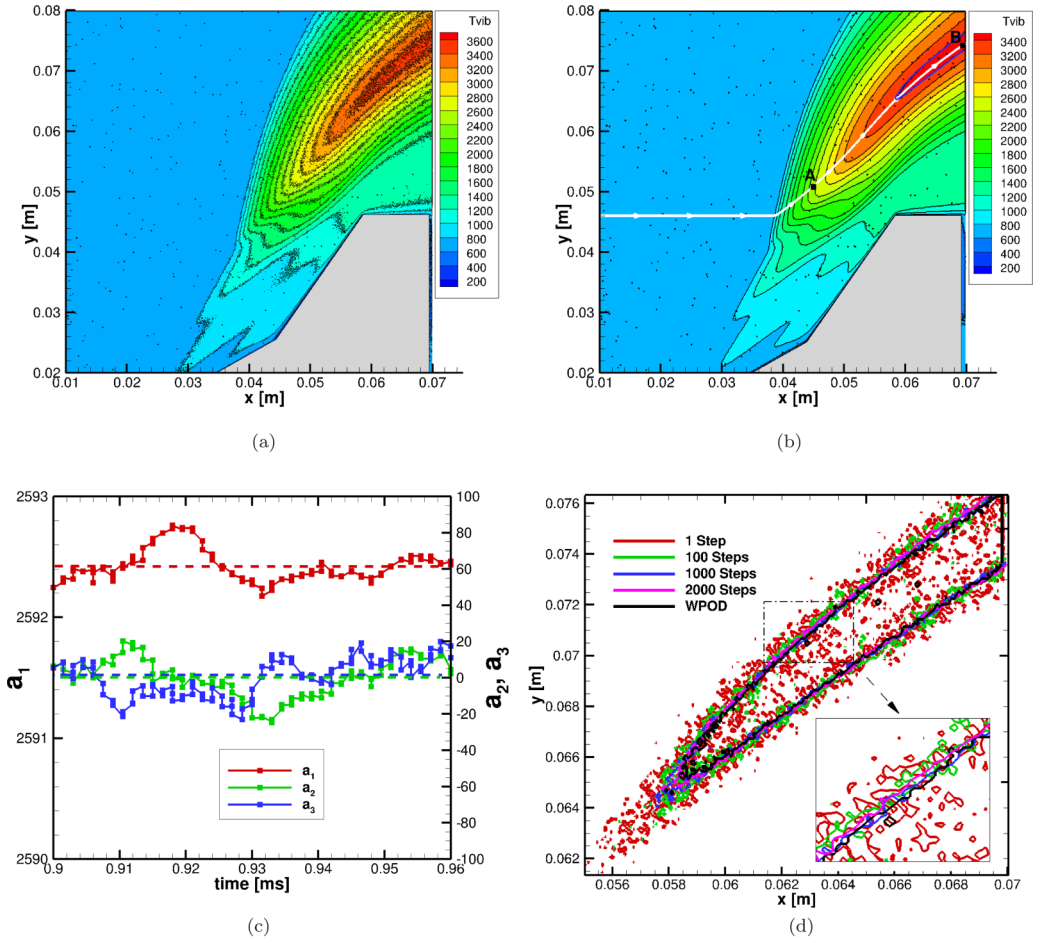

FIG. 4. Comparison of the spatial distribution of nitrogen vibrational temperatures [(a), (b), and (d)] using WPOD vs statistical sampling. (a) DSMC single time step sample, (b) Constructed using WPOD with 100 frames, (c) Temporal part of WPOD eigenmodes, and (d) Line comparison of the vibrational temperatures along the 3400 K constant line.

in this work are *unsteady*, ensemble averaging is performed using large numbers of particles per sampling cell. More details are provided in Appendix A and Ref. [10].

Turning to the double wedge, in Fig. 4(a) we show the vibrational temperatures of nitrogen molecules, corresponding to a single time-step sampling of a DSMC calculation using the numerical parameters discussed on Appendix A. The vibrational temperature field was selected since the degree of statistical fluctuations is larger in comparison to other flow field parameters, especially at the wedge shoulder where a strong thermal nonequilibrium is observed downstream of the bow shock. The steady-state solution, shown in Fig. 4(b), was constructed using only one WPOD eigenmode for 100 time windows, $N_{\text{pod}} = 100$, *after* the flow reached steady state. The WPOD analysis used the same spatial resolution of the DSMC background cells, i.e., the number of rows of the matrix in Eq. (3), n, was set equal to $800 \times 800 = 640{,}000$. The use of a single WPOD eigenmode is justified in Fig. 4(c), where it can be seen that the second and third modes have zero mean. Therefore, these higher modes are not included since their magnitude is on the order of the statistical noise. To clearly demonstrate the reduction in noise, Fig. 4(d) shows a comparison of the vibrational temperatures extracted along the $T_{\text{vib}} = 3400$ K contour in the strong bow-shock region

calculated using the WPOD approach versus values obtained using the usual DSMC sampling over different numbers of time steps. It can be seen that the WPOD method using 100 frames (black line) corresponding to Fig. 4(b) reduces the statistical noise to be as low as that of an average performed over 2 000 time steps of DSMC data. This shows that even apart from the need to use WPOD to characterize unsteady features in the DSMC simulations, it is an effective algorithm for reducing statistical fluctuation with at least an order of magnitude less data.

IV. TEMPORAL ANALYSIS USING THE WPOD APPROACH

As mentioned earlier, the time evolution in terms of spatial and temporal modes are considered for three systems, pure nitrogen, nonreacting air, and reacting air. The WPOD analysis was performed for 600 time windows after 0.6 ms of flow evolution for the nitrogen case, whereas it was found that 450 snapshots were sufficient to analyze the nonreacting air case, close to steady state. When chemical reactions are considered in the reacting air case, a larger number of time frames, 980, were required to capture all of the frequencies over a time period of 0.54–2.01 ms. The WPOD algorithm was performed for the nitrogen and nonreacting air cases over time intervals of 0.60–0.96 and 0.60–1.275 ms, respectively. These parameters will be referred to as the *baseline* case.

A. Analysis of time evolution of nitrogen flows

The macroscopic flow parameters, $\mathbf{q} = (u, v, T_{\text{trn}}, T_{\text{rot}}, T_{\text{vib}}, P)^T$, of the nitrogen flow are transformed to orthogonal modes in order to study the manner in which the flows come to steady state and to eliminate statistical fluctuations for trace quantities, as well. Figures 5–7 show the spatial variation of three POD modes and the corresponding temporal parts, respectively. It should be noted that only the first three modes are shown since the magnitude of the spatial parts for higher modes was found to be essentially zero and the temporal parts of higher modes also have a zero mean with respect to time, corresponding to statistical fluctuations. Therefore, three orthogonal modes are sufficient to represent the nitrogen flow this close to steady state, during the time interval of 0.6–0.96 ms.

Starting with the first mode, a comparison of Fig. 5(b) with Fig. 8(a), shows that the spatial part of the first mode for a flow macroparameter predicts the corresponding steady-state solution since the magnitude of the first temporal mode is at least an order of magnitude higher in comparison to the second and third modes, as can be seen in Fig. 7. Because of adverse pressure gradients at the second wedge surface, as can be seen in Fig. 5(c), the flow separation reduces both the x- and y-velocity field significantly in the vicinity of the hinge. Similarly, the strong shock interaction at $x = 0.055$ and $y = 0.045$ m results in elevated pressure values, as can be seen in the first of the pressure fields, as shown in Fig. 5. The first POD mode for the translational and rotational temperatures are found to be similar due to high relaxation rates between these modes, as can be seen by comparing Figs. 6(a) and 6(b). On the other hand, strong thermochemical nonequilibrium can be seen in Fig. 6(c), where the vibrational mode is excited only at the upper part of the second wedge.

The magnitude of the second and third modes for all macroparameters, on the other hand, is higher in the bow, separation, and transmitted shocks and the shear layer as can be seen in Figs. 5 and 6, indicating that most of the time variation of the flow this close to steady state occurs at these locations. This is consistent with our previous findings [33], where these flow structures were found to be strongly coupled to each other, emphasizing that any changes at these locations can have an influence on other locations. The second POD mode of Fig. 5 shows that the x-velocity component in the bow shock (i.e., all white region) decreases in an exponential decaying manner, as can be seen in Figs. 7(a) and 7(b), whereas the y-velocity component (strong dark region) shows the opposite trend due to momentum gain in the y direction. On the other hand, both the x- and y-velocity components can be seen to decrease along the shear layer (i.e., all white region) due to viscous effects. As shown in Fig. 5(c), at the separation point (S), the pressure values tend to increase (strong dark region) in

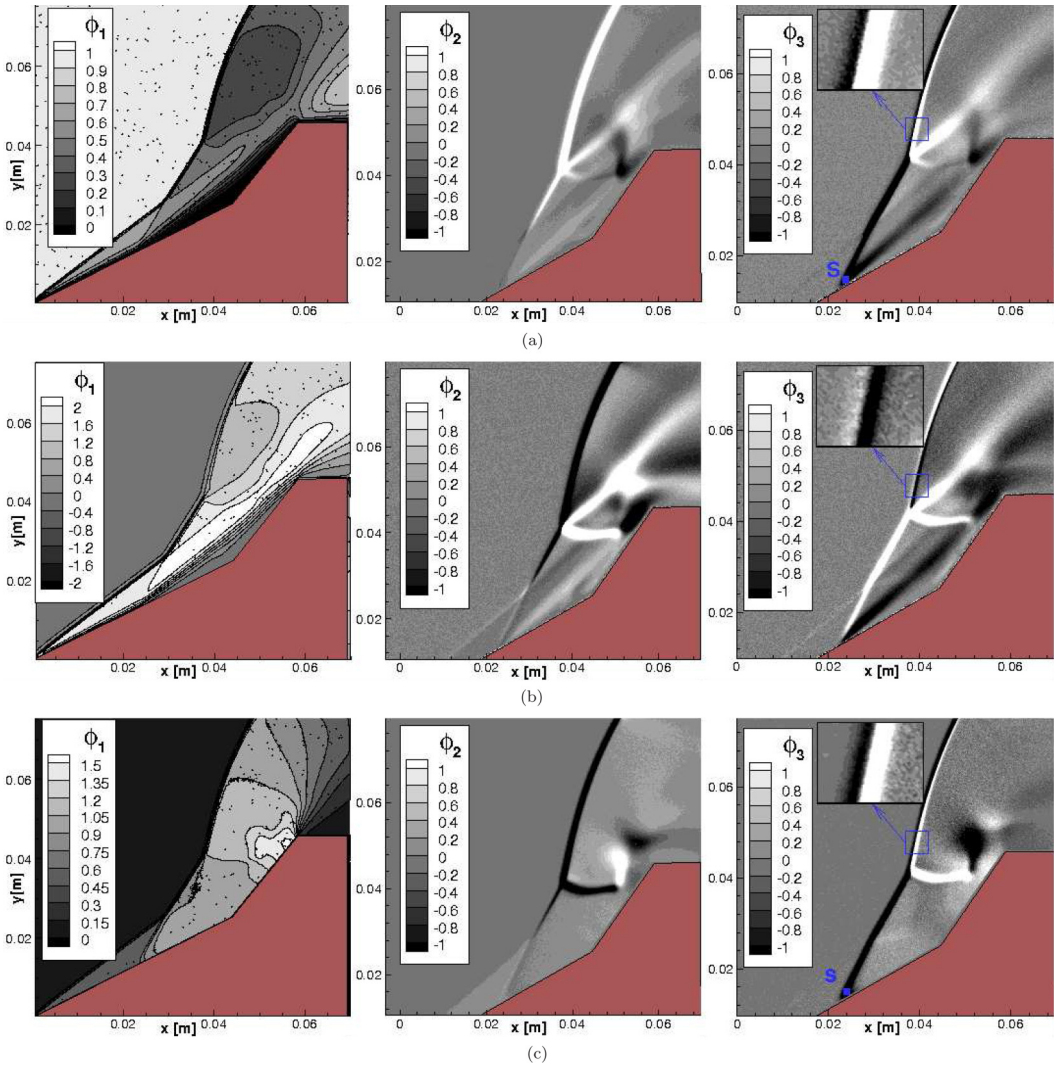

FIG. 5. Spatial distribution of POD modes for the velocity and pressure fields of nitrogen. (a) x-velocity, u, (b) y-velocity, v, and (c) Pressure, P.

the third POD mode. It should be noted that the dark color in the velocity fields corresponds to a decrease in the third mode, whereas the increase in the pressure values is due to the fact that the temporal part of the velocity third mode increases exponentially for times greater than 0.68 ms, in contrast to that for the pressure field, as shown in Fig. 7(c). Since the multiplication of the temporal and spatial parts determines the overall time characteristics of modes, the third mode of the pressure field increases after 0.68 ms at the separation point (S). The effect of thermal nonequilibrium can be seen by comparing the inset of Fig. 6(a) with Fig. 6(b). The sign change downstream of the bow shock for the second mode of the translational temperatures occurs since the translational energy decreases due to thermal relaxation with the rotational and vibrational modes. The temporal changes for the vibrational temperatures mostly occur in the shear layers, as shown in Fig. 6(c).

The temporal parts of the POD modes have similar time characteristics for different macroparameters, as can be seen in Fig. 7. Particularly, the first and second modes either increase or decrease exponentially in time, whereas the third mode shows both increasing and decreasing trends. An

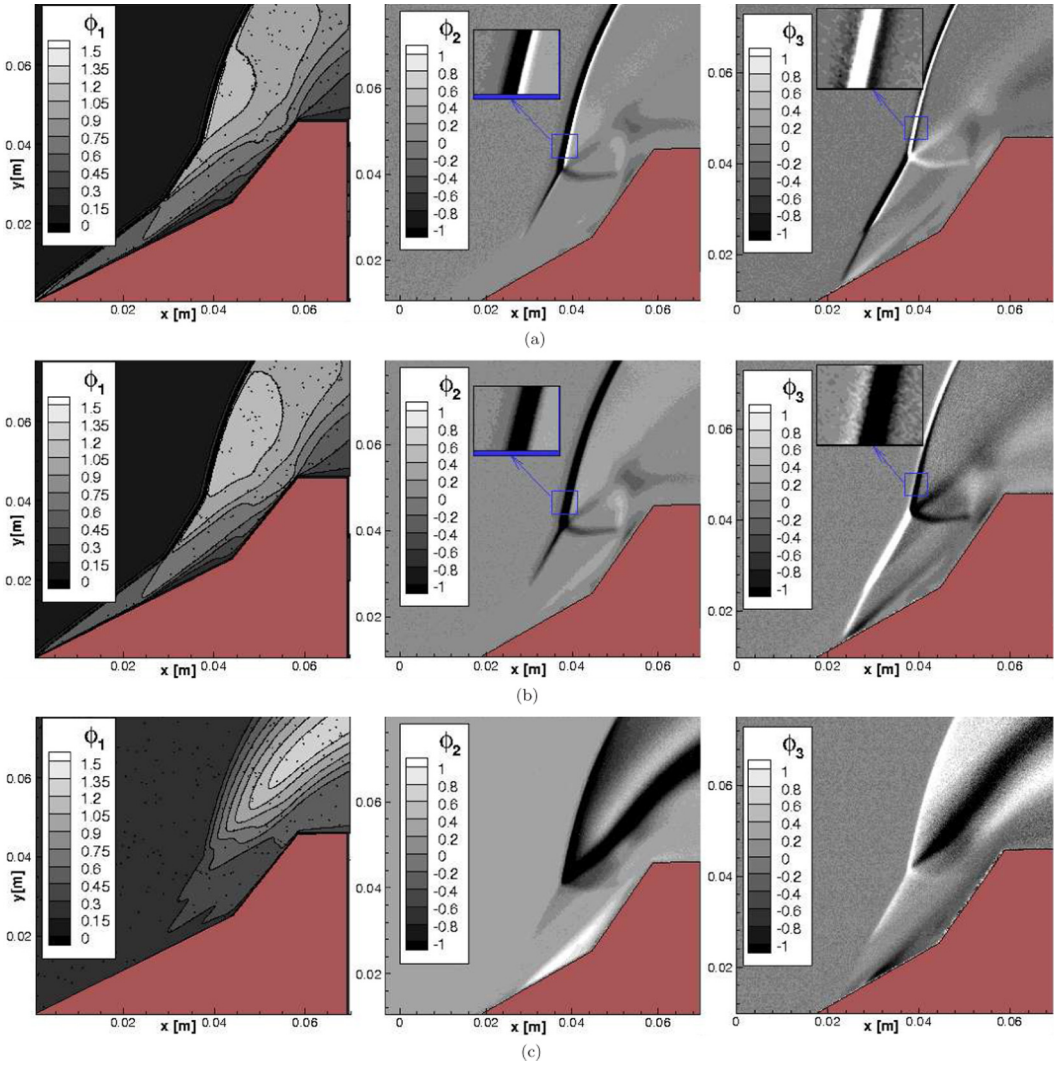

FIG. 6. Spatial distribution of POD modes for the temperature fields for the nitrogen case. (a) Translational temperatures, T_{trn}, (b) Rotational temperatures, T_{rot}, and (c) Vibrational temperatures, T_{vib}.

exponential curve fit of the form

$$\mathbf{q}(x, y, t) = \sum_{l=1}^{m} [k_l \phi_l(x, y) + A_l \, e^{\sigma_l t}] \tag{9}$$

is used between times $t_1 = 0.6$ and $t_2 = 1.05$ ms to obtain the decay rates σ for different macroparameters. The fit shows that the exponential decay rates, σ, for the x-velocity and translational temperature fields of the three POD modes are the same, as presented in Table III. Furthermore, using this fit data, the steady-state solution of each flow-field parameter, $\bar{\mathbf{q}}$, at $t \to \infty$ can be predicted. In other words,

$$\bar{\mathbf{q}} = \sum_{l=1}^{m} \phi_l k_l, \tag{10}$$

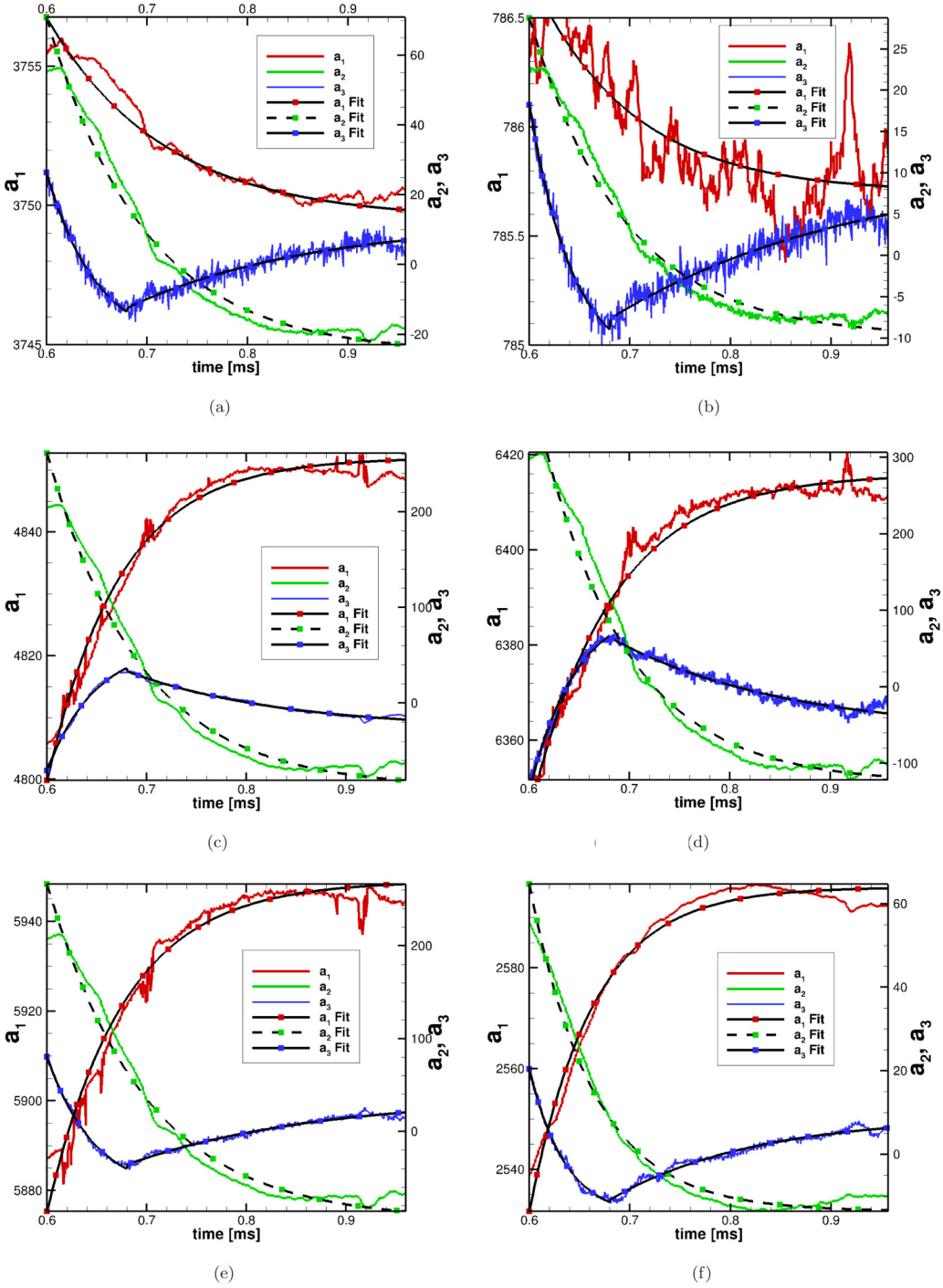

FIG. 7. Temporal parts of the POD modes for nonreacting nitrogen case. (a) x-velocity, (b) y-velocity, (c) Pressure, (d) Translational temperature, (e) Rotational temperature, and (f) Vibrational temperature.

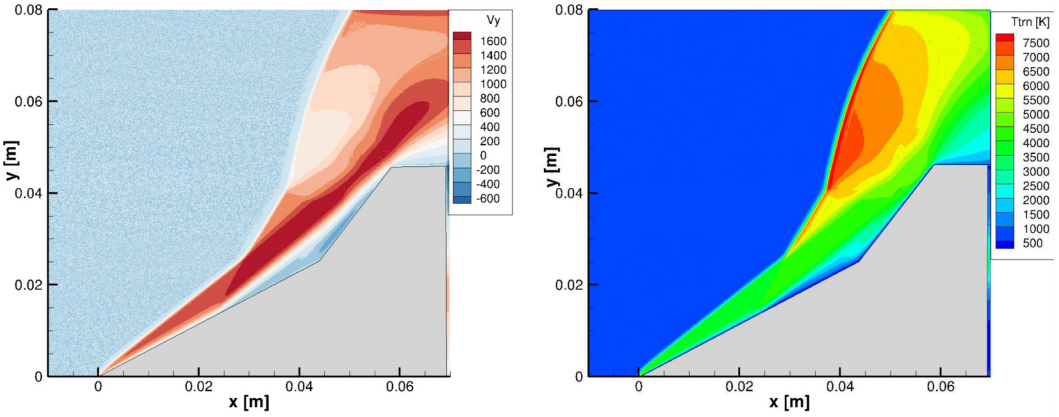

(a) (b)

FIG. 8. WPOD predictions of steady-state spatial distribution of the y-velocity and translational temperature fields for the nitrogen case. (a) y-velocity and (b) Translational temperature.

where the fit constants of k_l are presented in Table III for the translational and x-velocity fields and m is the number of POD modes required to represent the nitrogen flow and is equal to three. Using Eq. (10), the y-velocity field at steady state is calculated and presented in Fig. 8(a). Since the time variation of the temporal mode becomes almost zero, as shown in Fig. 7, it can be estimated that the flow is close to steady state after 1 ms. Therefore, 5 000 DSMC samples after 1.05 ms were taken to obtain a DSMC steady-state solution. A comparison of the WPOD with DSMC steady-state solutions is provided in Appendix B. The steady-state translational temperatures are calculated in a similar manner and are shown in Fig. 8(b).

With an understanding of how the POD modes characterize the time dependence of flow macroparameters, the calculated POD modes can be correlated with global modes, since in this work they are calculated when the flow is close to steady state. That is, the convergence of $\mathbf{q}(x, y, z, t)$ toward $\bar{\mathbf{q}}(x, y, z)$ can be estimated by the time evolution of temporal parts of POD modes. According to the residual algorithm of Theofilis [11,28], any flow macroscopic quantities can be represented by the linear superposition of a steady-state solution, and a small three-dimensional deviation from the steady state, denoted as residual, $\tilde{\mathbf{q}}(x, y, z, t)$, i.e.,

$$\mathbf{q}(x, y, z, t) = \bar{\mathbf{q}}(x, y, z) + \epsilon\tilde{\mathbf{q}}(x, y, z, t), \tag{11}$$

TABLE III. Coefficient of the data fitting for the nitrogen case given in Eq. (9).

Fit	q	t_1–t_2 [ms]	k	A	σ [1/ms]	GF[a]
1	u	0.60–0.96	3750	1.101×10^{4}	−12.17	0.94
2	u	0.60–0.96	−23.15	9.633×10^{4}	−11.55	0.98
3	u	0.60–0.68	−21.98	1.984×10^{7}	−21.52	0.97
3	u	0.68–0.96	11.58	−1319	−5.88	0.89
1	T_{trn}	0.60–0.96	6416	-1.064×10^{5}	−12.17	0.98
2	T_{trn}	0.60–0.96	−126	5.261×10^{5}	−11.5	0.98
3	T_{trn}	0.60–0.68	111.5	-1.014×10^{8}	−21.52	0.99
3	T_{trn}	0.68–0.96	−59.2	6778	−5.88	0.96

[a]Goodness of fit calculated based on adjusted R-square of MATLAB.

where ϵ is an infinitesimal quantity. Based on the fact that the coefficient of the residuals is independent of time (i.e., eigenmodes decomposition discussed in Ref. [11]), three-dimensional perturbations developing upon a steady laminar two-dimensional base state can be described by a perturbation of the form:

$$\tilde{\mathbf{q}}(x, y, z, t) = \hat{\mathbf{q}}(x, y)\mathrm{e}^{\mathrm{i}[\beta z - \omega t]} + \mathrm{c.c.}, \tag{12}$$

where the wave-number parameter, β, is defined as $2\pi/L_z$, L_z being the spanwise extent of the three-dimensional domain. In planar geometries and a temporal analysis framework [38], the β parameter is taken to be a real number whereas the eigenmodes, $\hat{\mathbf{q}}(x, y)$, and ω may be complex. In the present analysis, special attention is paid to two-dimensional perturbations only, which correspond to $\beta = 0$. Therefore, Eq. (12) can be rewritten in a two-dimensional context:

$$\mathbf{q}(x, y, t) = \bar{\mathbf{q}}(x, y) + \epsilon\,[\hat{\mathbf{q}}_r \cos\omega_\mathrm{r} t - \hat{\mathbf{q}}_i \sin\omega_\mathrm{r} t]e^{\sigma t}, \tag{13}$$

where $\sigma = \omega_i$ is the damping rate and ω_r is the circular frequency term. It should be noted that Eqs. (9) and (13) are in the same form when the waves are stationary ($\omega_\mathrm{r} = 0$). Therefore, the exponential terms presented in Table III for the temporal parts of the POD modes can be represented as the decay rates of global modes, σ. Based on this, the decay rate of the least damped eigenmode, $\sigma_{l=3}$, can be estimated as -5.88 ms^{-1}. In our previous works [10,33], we observed that the magnitude decay rate of the least damped eigenmode decreases with Reynolds number, which in turn increases the required time to reach steady state. Consistent with this, the magnitude of the decay rate for the nitrogen case is larger since the unit Reynolds number given in Table I is lower than those given in Ref. [10]. Additional numerical studies were performed to verify that the damping rates are independent of the number of snapshots, as explained further in Sec. V.

B. Effects of multiple species on POD modes

After examining the time characteristics of nitrogen flow, the spatial and temporal characteristics of nonreacting air flow over the same geometry is investigated in order to understand the origin of the sinusoidal fluctuations shown in Fig. 2(b). An analysis similar to the nitrogen case was performed with 450 snapshots between 0.60 and 1.275 ms. It should be noted that since chemical reactions are not active for this case, the macroparameters of nitrogen and oxygen molecules are sampled independently and the WPOD algorithm was applied separately for each of the macroparameter of these species.

Figure 9 shows the POD modes of the translational temperature of nitrogen molecules in this flow mixture. As opposed to the pure nitrogen case where three orthogonal modes were sufficient to represent the time evolution of the flow after 0.6 ms, now nine modes are required for this case, although the magnitude of the last two spatial modes is small. As can be seen by comparing the first mode of Fig. 9(a) to Fig. 6(a), the spatial distribution of the translational temperatures is found to be similar and since the first mode outlines the general features of the steady-state solution it is expected that the spatial distribution of the translational temperatures at steady state will be similar for the nitrogen and nonreacting air cases. As before, for higher modes, most of the spatial variations are found to be in the bow, separation, and transmitted shocks and along the shear layer. In particular, the magnitude of POD modes is found to be relatively larger at location R, where the transmitted shock interacts with the boundary layer of the second wedge. The aforementioned sign change in the bow shock due to the thermal nonequilibrium is also seen in the translational temperature third mode (Fig. 9). Similar to the third mode of the nitrogen case, the fourth mode of the nonreacting air case demarcates the separation shock and the shear layer. Consistent with nitrogen, Fig. 10 shows that the magnitude of the second and higher POD modes for the x-velocity field is higher at the shock interaction locations. Note that the other macroparameters for nitrogen as well as oxygen show similar characteristics to the pure nitrogen case.

Figure 11 shows the corresponding temporal modes for the translational temperatures and the x-velocity field. In contrast to the nitrogen case where three temporal POD modes damped out in an

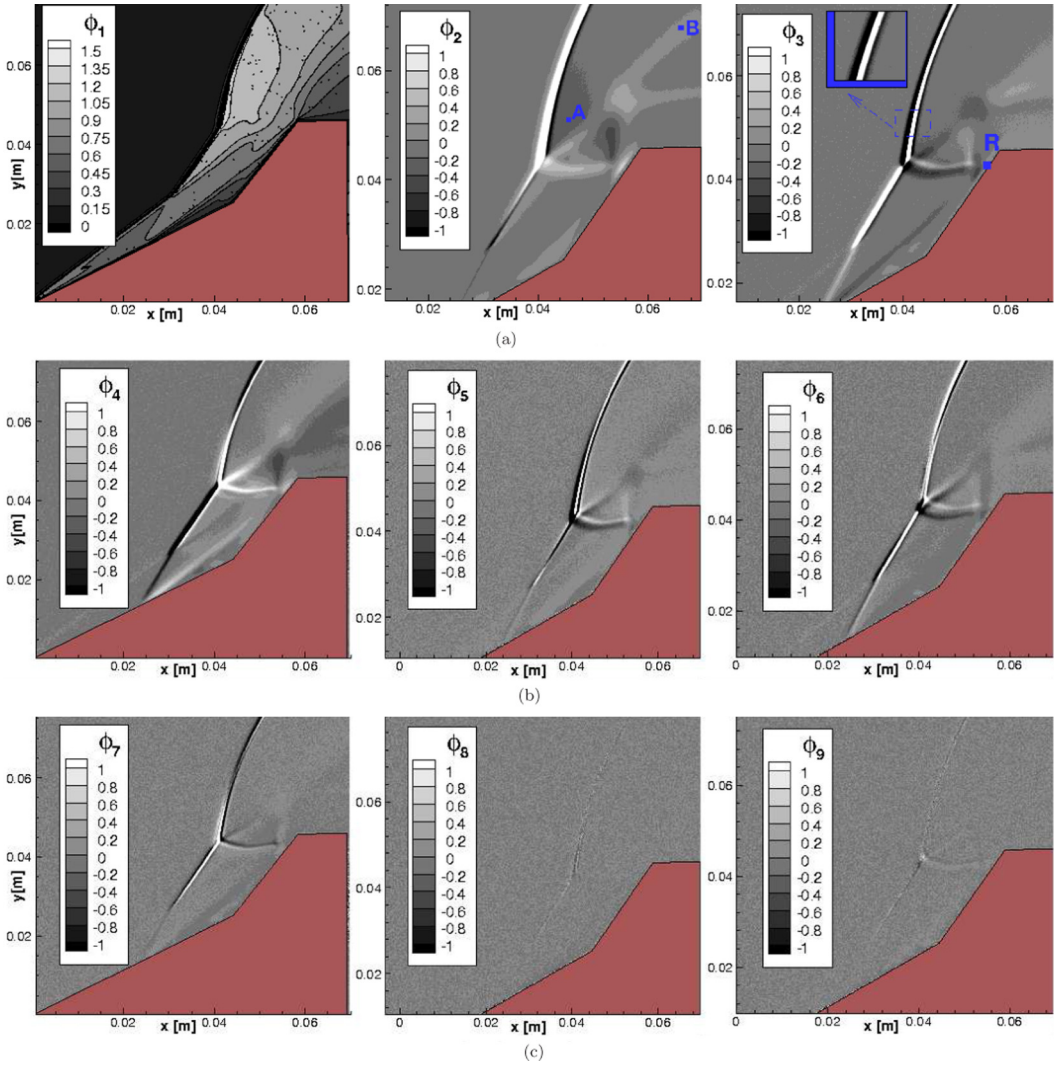

FIG. 9. Spatial parts of the POD modes for the translational temperatures for the nonreacting air case. (a) First three modes, (b) 4th, 5th, and 6th modes, and (c) 7th, 8th, and 9th modes.

exponential manner, there are sinusoidal fluctuations for the nonreacting air case consistent with the numerically probed DSMC data shown in Fig. 2. Figures 11(a) and 11(b) show the time evolution of the most energetic three modes and the corresponding fitted curves obtained using the form

$$\mathrm{a}(t) = k + \sum_{i=1,2} [(Am_i \cos(\omega_i t) - An_i \sin(\omega_i t))\, e^{\sigma_i t}], \tag{14}$$

where the coefficients are presented in Table IV for the translational temperature of nitrogen. Table IV shows that Eq. (14) well represents the temporal POD mode data for the first four POD modes, although some discrepancies are observed for the higher modes where the goodness of fit deviates from unity. It should be noted that the damping rates of σ_1 and σ_2, and the circular frequencies, ω_1 and ω_2, of each fit are found to be essentially the same for nitrogen and oxygen but the coefficients of k, Am_1, Am_2, An_1, and An_2 vary for each flow-field parameter.

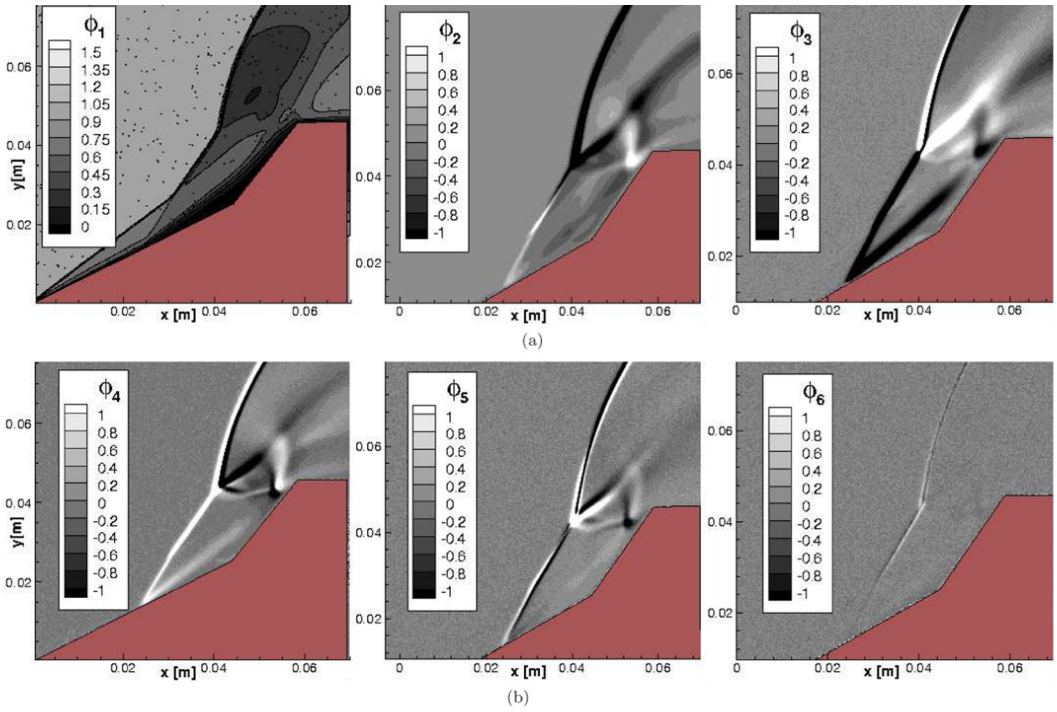

FIG. 10. Spatial parts of POD modes for the x-velocity field for the nonreacting air case. (a) First three modes and (b) 4th, 5th, and 6th modes.

As discussed previously, the POD modes can be used to calculate global modes at steady state or any time for each flow-field quantity. Since all damping rates given in Table IV are negative, the flow reaches steady state for the nonreacting air case and the calculated steady-state solution using Eq. (10) for the translational temperatures of nitrogen is shown in Fig. 12(a). Furthermore, a comparison of the translational temperature contours for the nonreacting air versus nitrogen cases, Figs. 12(a) versus 8(b), shows that in the nonreacting air case molecular nitrogen has smaller regions of peak temperatures compared to the pure nitrogen case. This is due to the effect of N_2 translational-vibrational relaxation due to collisions with O_2. Since Eqs. (13) and (14) have the same time dependence, the POD modes can also be used to obtain global modes corresponding to the two-dimensional traveling waves. Using Eqs. (7), (13), and (14) we can express the real and

TABLE IV. Coefficients of curve fitting given in Eq. (14) for the translational temperatures of nitrogen for the nonreacting air case. The bold and italicized numbers represent the primary and the least damped eigenmodes, respectively, here and in subsequent tables.

Fit	k	Am_1	Am_2	An_1	An_2	ω_1	ω_2	σ_1	σ_2	GF
1	5978	**78.34**	4.647×10^5	**−666.6**	2.634×10^5	**22**	−19.7	**−3.891**	−18	0.99
2	−66.33	**905.5**	-8.784×10^6	**−3640**	-7.648×10^7	**22**	21.47	**−3.891**	−18.5	0.99
3	12.79	**23.74**	-4.516×10^6	**−3967**	7.651×10^7	**22**	−32	**−3.891**	−18.85	0.98
4	17.98	**3202**	4.964×10^6	**−1625**	2.457×10^7	**22**	32	**−3.891**	−18.00	0.98
5	4.807	***81.53***	2970	***8.106***	-1.838×10^4	*22*	58.19	***−1.211***	−8.044	0.64
6	1.721	-5.804×10^7	6.057×10^8	3.115×10^7	-1.384×10^8	27.73	58	−20.82	−23.6	0.8
7	−2.129	84.32	−254.1	−80.5	−275.6	27	44	−1.676	−2.7	0.57

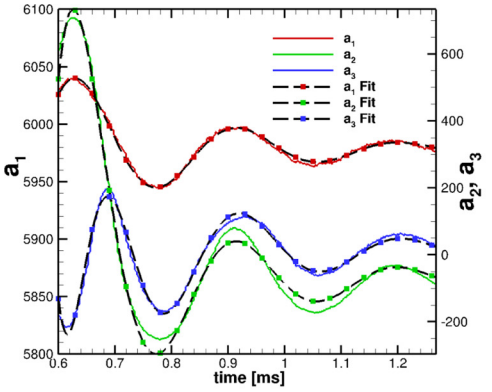

(a)First three modes

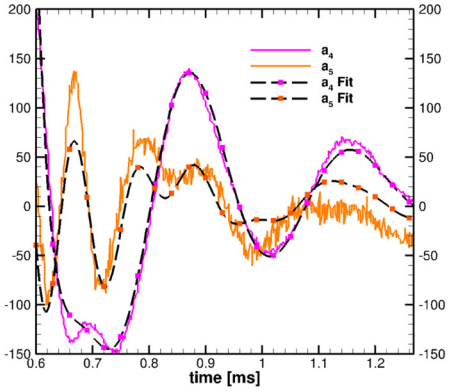

(b)4^{th} and 5^{th} modes

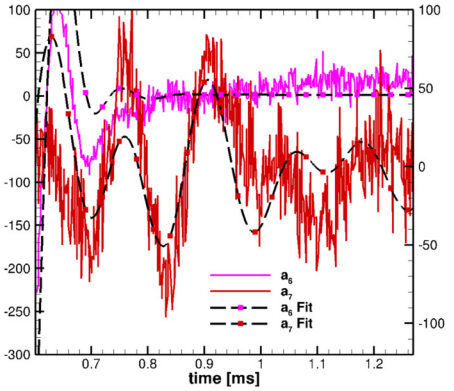

(c)6^{th} and 7^{th} modes

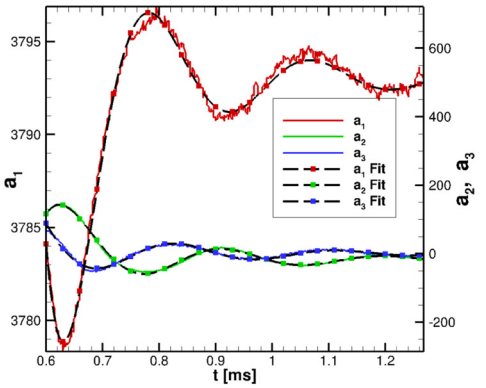

(d)First three modes

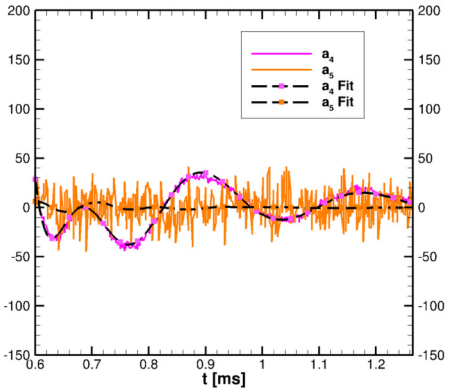

(e)4^{th} and 5^{th} modes

FIG. 11. Temporal parts of the modes for the nonreacting air case: panels (a), (b), and (c) show the translational temperature for nitrogen and panels (d) and (e) show the x velocity for oxygen molecules.

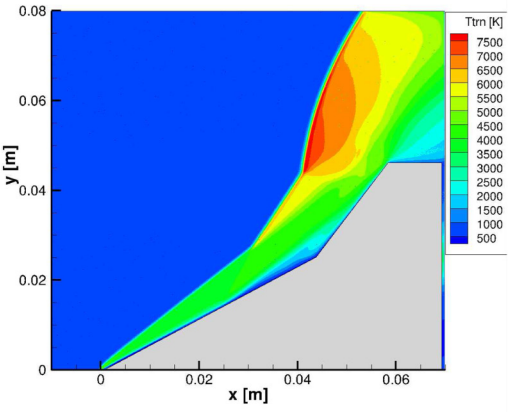

(a)Steady-state solution

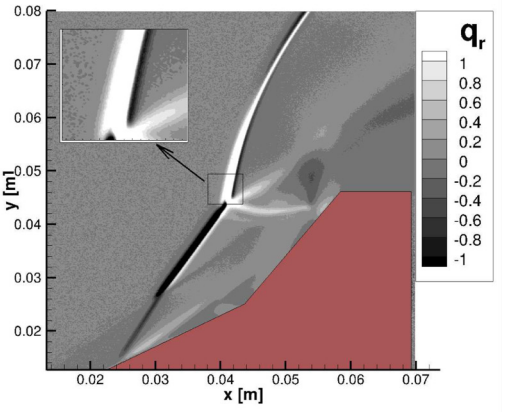

(b)Real part of the most dominant mode, $\hat{\mathbf{q}}_r$

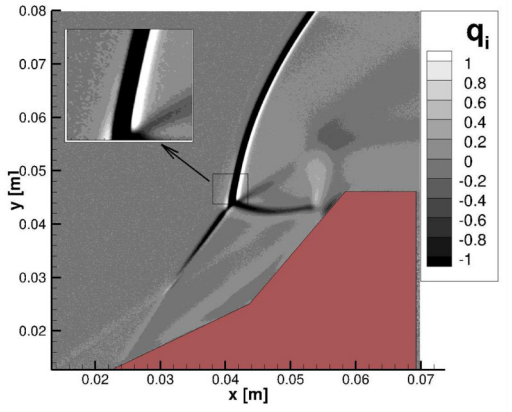

(c)Imaginary part of the dominant mode, $\hat{\mathbf{q}}_i$

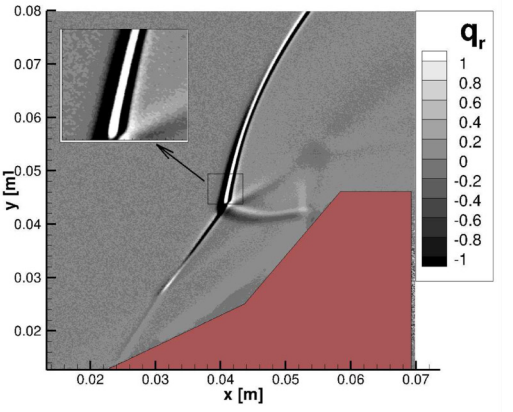

(d)Real part of the least damped mode, $\hat{\mathbf{q}}_r$

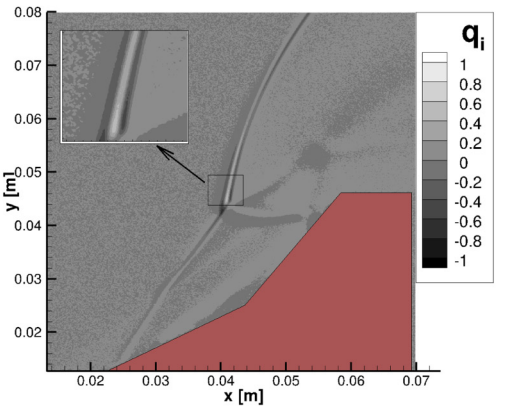

(e)Imaginary part of the least damped mode, $\hat{\mathbf{q}}_i$

FIG. 12. Spatial distribution of the translation temperatures at steady state and amplitude functions of the nonreacting air case. Note that panels (b) and (c) are normalized with 5 000 K whereas panels (d) and (e) are normalized with 100 K.

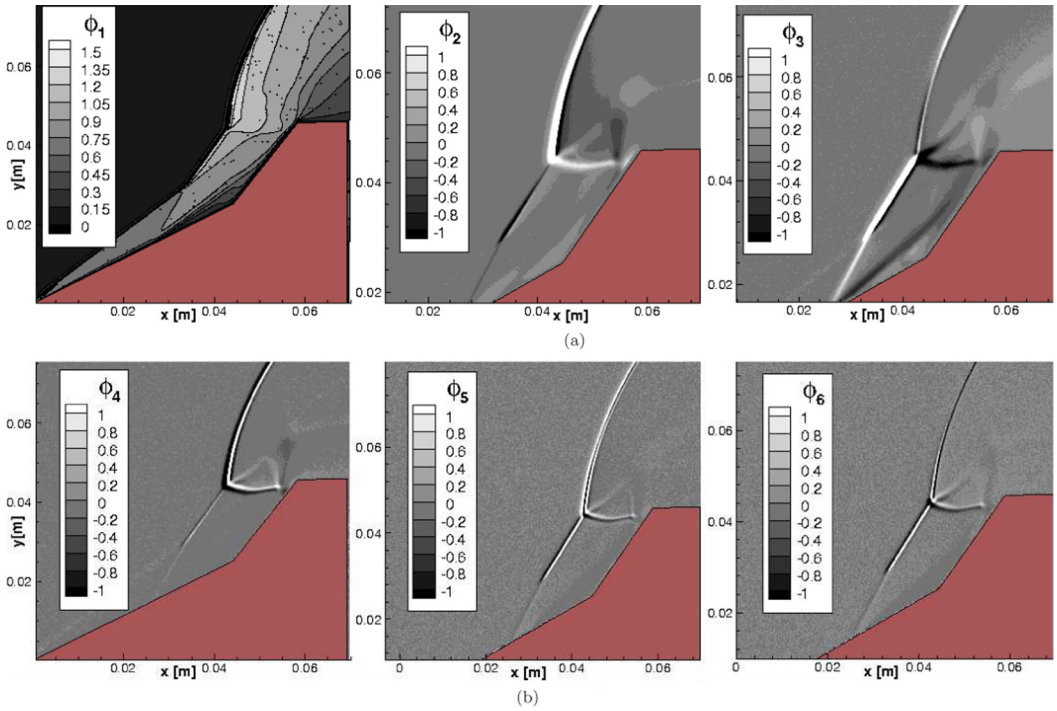

FIG. 13. POD modes for the translational temperatures of nitrogen for the reacting air case. (a) Spatial first three modes and (b) Spatial 4th, 5th, and 6th modes.

imaginary parts of the amplitude functions as

$$\hat{q}_r = \sum_{l=1}^{m} \phi_l(x,y) A m_l \quad \text{and} \quad \hat{q}_i = \sum_{l=1}^{m} \phi_l(x,y) A n_l. \tag{15}$$

The real and imaginary parts of the eigenmode that corresponds to the given four POD modes are calculated using Eq. (15) and are shown in Figs. 12(b) and 12(c), respectively. It should be noted that since the primary four modes have a common damping rate and circular frequency (see Table IV), most of dynamical behavior is determined by these four POD modes.

It can be seen that the magnitude of both real and imaginary parts is higher at the bow, separation, and transmitted shocks and shear layers, consistent with the trend shown by the POD modes and the interactions of the transmitted shock with the boundary and shear layers are distinctive in both real and imaginary amplitude functions. Lastly, the least damped eigenmode is determined based on the highest decay rates (i.e., lowest in magnitude) of the POD modes, using the fifth fit data in italic given in Table IV and the corresponding amplitude functions are shown in Figs. 12(d) and 12(e), respectively. Since the contribution of this POD mode to the dynamical behavior of the flow is small, the magnitude of the amplitude functions is also smaller in comparison to the most dominant global mode shown in Figs. 12(b) and 12(c). However, for flows at even higher Reynolds numbers, these modes may contribute to even greater flow unsteadiness.

C. Effects of chemical reactions on POD modes

Since chemical reactions remove heat from the flow, we expect that they will have an important effect on the way hypersonic, separated flows reach steady state. In this section, we examine how the two chemical reactions expected to be important for this Mach number, Eqs. (1) and (2), effect the

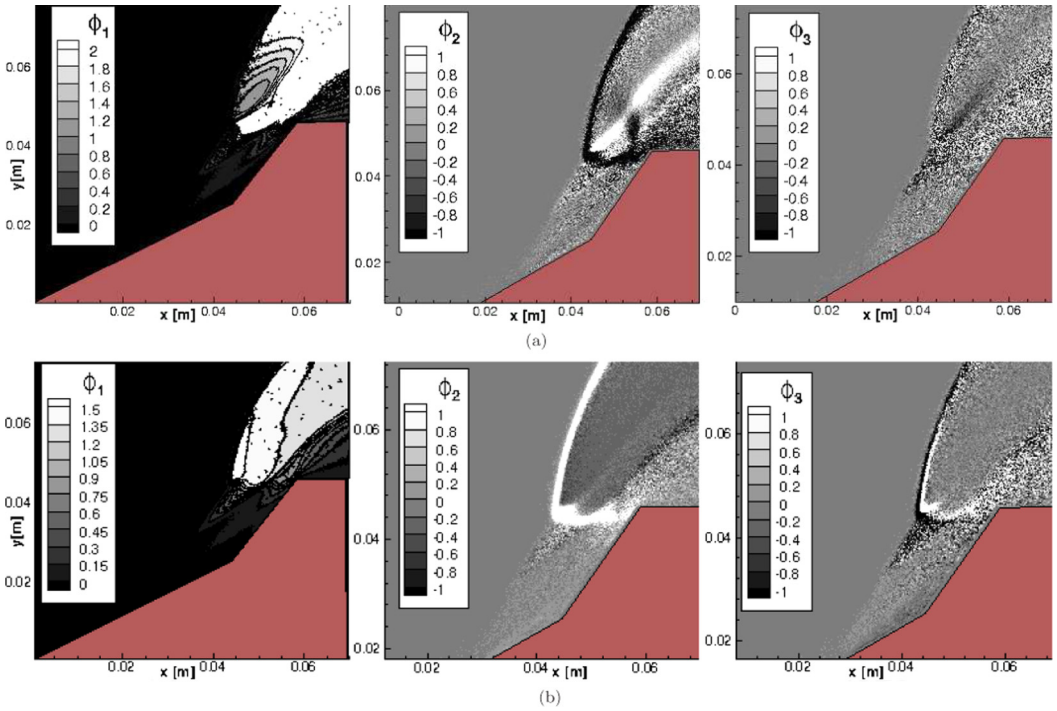

FIG. 14. Spatial POD modes for the trace species of N and NO for the reacting air case. (a) x-velocity for N atoms and (b) Vibrational temperature of NO molecules.

POD and global modes. Similar to the previous case, the WPOD method was applied to the time-variant DSMC data and the spatial and temporal modes for each macroparameter were determined for the five chemical species of N, O, N_2, O_2, and NO. Figure 13 shows the POD modes of the translational temperatures for nitrogen molecules. Similar to the previous cases, the most dynamic parts close to steady state are found to be in the bow, separation and transmitted shocks, and the separation region.

A comparison of the translational temperatures for the reacting versus the nonreacting air mixture, Figs. 13 with 9, shows that the spatial distribution of the POD modes is similar in many ways. In particular, the spatial distribution of the second mode of both cases is similar in the shock regions. Also, the shear layer in the vicinity of the separation region and the reflected shock can be seen to be active in the third mode of both cases. However, some differences are observed downstream of the bow shock and in the shear layer due to endothermic chemical reactions. In particular, as can be seen in the second mode of Fig. 9, the dark gray region downstream of the bow shock (i.e., in the vicinity of location A) is more localized in comparison to that for the reacting air case and the white region along the shear layer (i.e., location B) extends further downstream for the nonreacting air case.

The spatial variation of the POD modes for trace species of N and NO, the products of the chemical reactions, are shown in Fig. 14. As expected, the first three modes are active downstream of the bow shock where the chemical reactions take place since the translational temperatures are high in this region. Although the statistical noise seen in the second and third modes of Fig. 14 somewhat obscures the general features of the modes, most of the spatial variations for the velocity field of N and the vibrational temperatures of NO are found to be in the bow shock and shear layer. The statistical fluctuations can be attributed to DSMC sampling cells having fewer number of particles.

The temporal parts of the POD modes and the corresponding fitted curves are shown in Fig. 15. Similar to the nonreacting air case, the fitted curves for the primary three modes are found to be

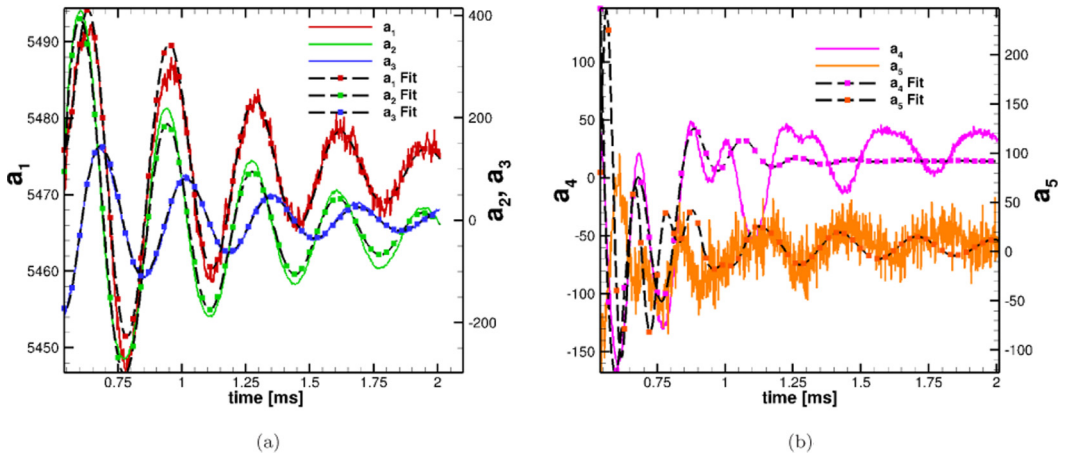

FIG. 15. Temporal modes of the translational temperature for nitrogen molecules for the reacting air case. (a) First three modes and (b) 4th and 5th modes.

in excellent agreement with the fit goodness of close to unity, as presented in Table V. On the other hand, some discrepancies are observed between the fitted lines and the POD data especially after 1 ms for higher modes and can be attributed to statistical fluctuations of the DSMC method. Nonetheless, since the main features of the reacting air are determined by these primary modes, based on the fact that the corresponding amplitudes are approximately an order of magnitude higher, the effects of these discrepancies for higher modes on the steady state solution and amplitude functions are negligible.

Similar to the nonreacting air case, the steady-state solution for the reacting air case was calculated using Eq. (10) based on the spatial and temporal parts of the POD modes given in Table V. Figure 16(a) shows the spatial distribution of the translational temperatures for nitrogen molecules at steady state. A comparison of Fig. 16(a) with Fig. 12(a) shows that although general features of the flow field are similar for both cases, the translational temperatures are reduced for the reacting air case because of the endothermic dissociation and the exchange reactions. Similar to the nonreacting air case, the amplitude functions were calculated using Eq. (15) and are shown in Figs. 16(b) and 16(c). The magnitude of the amplitude functions is larger at the separation, bow shocks, and transmitted shocks, consistent with the nonreacting case shown in Figs. 12(b) and 12(c). This emphasizes that the sinusoidal fluctuations are dominant at these locations.

The ultraviolet emission spectroscopy and laser-induced fluorescence of nitric oxide produced in hypersonic, unsteady flows may provide important measurements of flow temperatures and velocities. Further complicating the use of these flow diagnostics is the fact that generally experimental run times are less than 2 ms, which makes a one-to-one comparison between simulations and

TABLE V. Coefficient of the data fitting given in Eq. (14) for the translational temperatures of the reacting air case.

Fit	k	Am_1	Am_2	An_1	An_2	ω_1	ω_2	σ_1	σ_2	GF
1	5473	**50.14**	-3.424×10^4	**69.92**	4.221×10^4	**18.75**	22	−1.716	−13.97	0.97
2	−20.19	**606.3**	1.057×10^8	**939.4**	-8.36×10^7	**18.88**	22	−1.716	−24.98	0.99
3	−0.5651	**451.8**	-7.572×10^7	−134.1	9.136×10^7	**18.75**	22	−1.716	−25.69	0.99
4	14.63	−9172	−4219	1.836×10^4	−441.8	−10	32	−7.4	5.54	0.74
5	−0.6585	-1.556×10^4	212.1	-2.008×10^4	−257	34.14	37.27	−8.945	−3.2	0.33
6	0.7595	240.4	−7.306	−61.62	2.824	−40	22	−2.726	−0.7	0.30

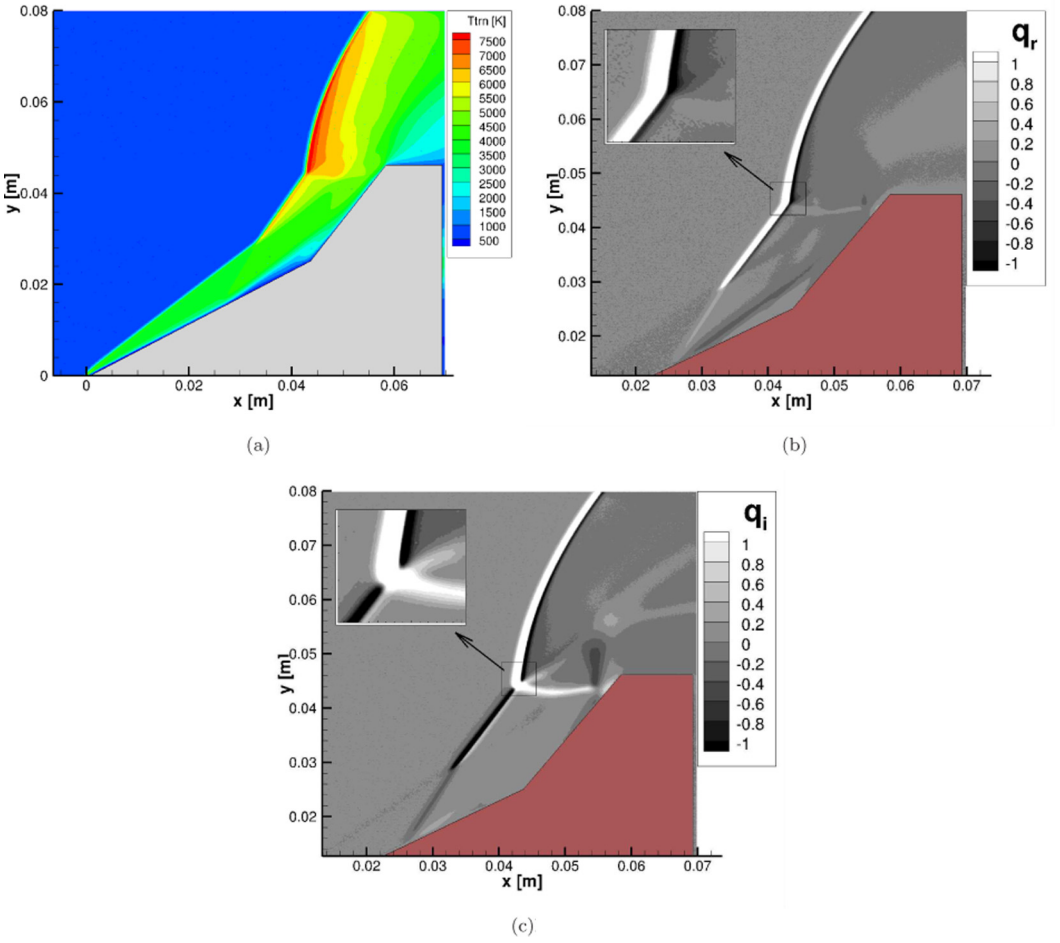

FIG. 16. Spatial distribution of the translational temperatures at steady state and amplitude functions normalized with 1000 K for the reacting air case. (a) Translational temperatures at steady-state, (b) Real part of the most dominant mode, $\hat{\mathbf{q}}_r$, and Imaginary part of the dominant mode, $\hat{\mathbf{q}}_i$.

experiments challenging due to the fact that hypersonic separated flows may not reach steady state in such a short duration. Figure 17 demonstrates the use of the WPOD method to predict the time-accurate spatial distribution of NO vibrational temperatures close to steady state and comparison of Figs. 17(a) and 17(b) shows that the statistical fluctuations are diminished substantially. It was found that the decay rate and circular frequency of temporal POD modes for NO (not shown) are essentially the same with that of the bulk flow, as expected. Therefore, although there is some remaining statistical noise even after applying WPOD, it does not influence the definition of the POD modes.

A comparison of Figs. 17(b) with 4(b) shows that the spatial distribution of the vibrational temperatures of NO is substantially different from that of N_2. In particular, the maximum vibrational temperatures for NO molecules occurs at location A of Fig. 17(b) downstream of the bow shock, whereas the highest vibrational temperatures for nitrogen takes place even further downstream at location B shown in Fig. 4(b). It should be noted that NO is initially produced by the exchange reaction downstream of the bow shock and the translational and internal energies of nascent NO molecules are distributed based on the equipartition theorem. Therefore, the NO vibrational temperatures, as well as rotational and translational temperatures, are similar to the translational temperatures of nitrogen in the bow shock region, as shown in Fig. 16(a).

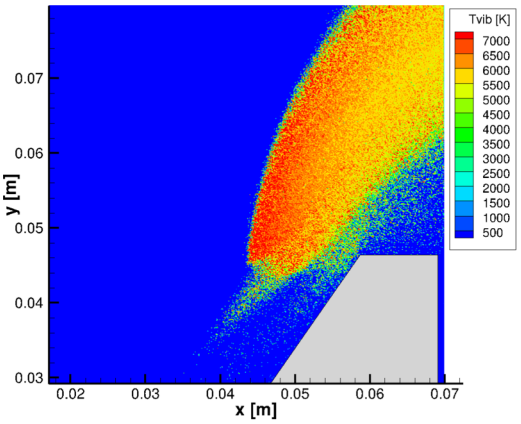

(a)DSMC data at 2 ms

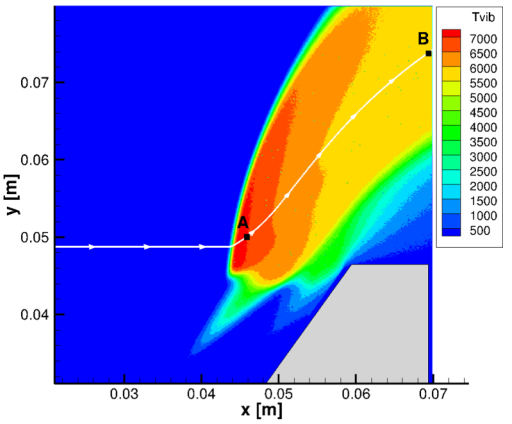

(b)Steady state calculated using the WPOD method

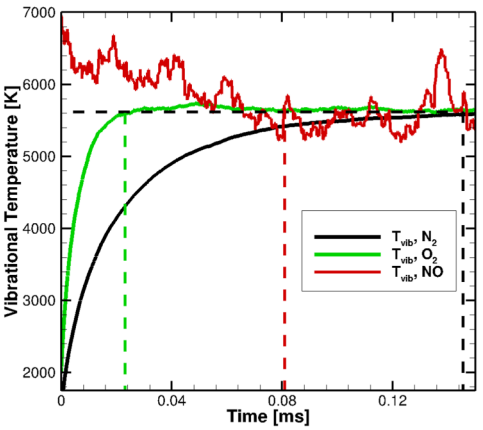

(c)Time relaxation of vibrational temperature

FIG. 17. Spatial distribution of the vibrational temperatures of NO: (a) single time step, (b) at steady state, and (c) temporal evolution of the vibrational temperatures of molecules at location A.

To investigate the thermal relaxation time more closely, a zero-dimensional DSMC relaxation calculation was performed using the flow conditions at location A. As described in Appendix A, the Larsen-Borgnakke (LB) model was used to determine the probability of vibrationally energy exchange for each collision based on a vibrational relaxation probability defined as $P_v = 1/Z_v$, where Z_v is the vibrational relaxation number [Eq. (A3)] and is a function of the characteristic temperature, θ, and temperature. Since P_v depends on the colliding species pair, the corresponding relaxation time to equilibrium will also be different for each species in the flow. Figure 17(c) shows the temporal evolution of the vibrational temperatures of nitrogen, oxygen, and nitric oxide molecules. Initially, due to the cold free-stream temperature and the strong bow shock, the vibrational temperatures of oxygen and nitrogen molecules are low with an approximate value of 2 000 K, whereas the vibrational temperature of nitric oxide molecules is 7 000 K and the calculations show that all relax to the local equilibrium value of about 5 600 K. Since the Z_v for nitrogen is the highest, it relaxes to the equilibrium temperature about five times more slowly than O_2, and two times slower than NO. Note that based on a distance of 0.035 m along the streamline from A to B and the average bulk velocity of 1300 ms^{-1}, the flow takes around 0.027 (dashed green) ms to travel from A to B. As can be seen in Fig. 17(c), the vibrational temperatures of

nitrogen molecules at 0.027 ms is about 4000 K, which is consistent with the value at location B of Fig. 4, although the flow is expanding and the chemical reactions are taking place. Also, it can be seen that the flow needs about 0.08 ms to reach thermal equilibrium. This implies that the flow is in a nonequilibrium state within the computational domain and would need to travel three times longer than 0.035 m to reach equilibrium which would be beyond the domain.

D. Effects of thermochemical nonequilibrium on flow evolution

The effects of thermochemical nonequilibrium are prominent in the temporal parts of the POD modes. As shown in Table V, the primary modes have a common decay rate of 1.716 ms^{-1} with a circular frequency of 18.75 ms^{-1} for the reacting air case whereas the corresponding decay rate and circular frequency are 3.891 and 22 ms^{-1} for the nonreacting air case in Table IV. This shows that the modeling of chemical reactions decreases the magnitude of the decay rate almost by a factor of 2, which in turn results in an increase in the required time to reach steady state. A similar trend can also be seen in comparing the nitrogen and nonreacting air cases. The effect of multiple species results in a decrease of the magnitude of the decay rate. In particular, the decay rate of the least damped eigenmode for the nitrogen case is -5.88 ms^{-1}, as presented in Table III.

This important finding is consistent with the probed data shown in Fig. 2, where it can be seen that the nitrogen case almost reaches steady state after 0.8 ms. For the nonreacting air case, most of the disturbances are damped out at 1.2 ms, whereas a large amount of sinusoidal disturbances are still active at this time for the reacting air case. Based on the decay rates, the required time to reach steady state can be estimated. In this work, the flows are assumed to reach steady state when the residuals given in Eq. (11) reach 0.3% of its initial value. Therefore, the estimated times for steady state are 1.0, 1.5, and 3.4 ms for the nitrogen, nonreacting air, and reacting air cases, respectively. Moreover, the angular frequencies of 18.75 and 22 ms^{-1} for reacting and nonreacting air cases correspond to frequencies of about 3 and 3.5 kHz using the relationship of $\omega = 2\pi f$. These frequencies are found to be consistent with the dominant frequency of 2 kHz observed in the bow shock and separation shocks motion of a nonreacting Mach 16 nitrogen flow over a double cone (see Ref. [33] for details).

The reason why multiple species and chemical reactions alter the flow time characteristics is primarily due to the different translational temperatures downstream of the bow shock that result from internal relaxation rates and endothermic reactions. As can be seen in Figs. 8(c), 12(a), and 16(a), the translational temperature is the highest for the nitrogen case, which increases the size of the separation region compared to the nonreacting and reacting air cases. This in turn alters the bow shock standoff distance and the location of the triple point (T). The calculated viscous dissipation rates and estimated shock standoff distances are shown for the three cases along with insets of dynamic viscosity based on Sutherland's formula in Fig. 18 using the steady-state translational temperature fields shown in Figs. 8(c), 12(a), and 16(a), for the nitrogen, nonreacting air, and reacting air cases. It should be noted that the spatial distribution of translational temperatures and viscosities in the vicinity of the separation point and over the first wedge were found to be similar for all these cases. As shown in Fig. 18(a), the nitrogen case has a larger shock standoff distance than the air cases, consistent with the findings of experiments [4] at higher densities. The larger separation region and increased region of dark red and orange flooded contours for high viscosity will have a stabilizing effect on the flow due to larger viscous dissipation rates, consistent with Ref. [39]. Therefore, this reduces the time to come to steady state even though the recirculation region is larger. The nonreacting air case, shown in Fig. 18(b), has larger peak viscosity values due to the introduction of oxygen into the flow, which has a 20% larger viscosity value at a reference temperature of 1000 K (see Table II). As Fig. 18 shows, the overall viscous dissipation rates decrease from the nitrogen to reacting air case and have a major effect on the time required to reach steady state for the three cases.

Finally, the determination of when steady state has been reached has an important numerical savings as well. Approximately 11 000 and 45 000 CPU hours were saved for the nonreacting

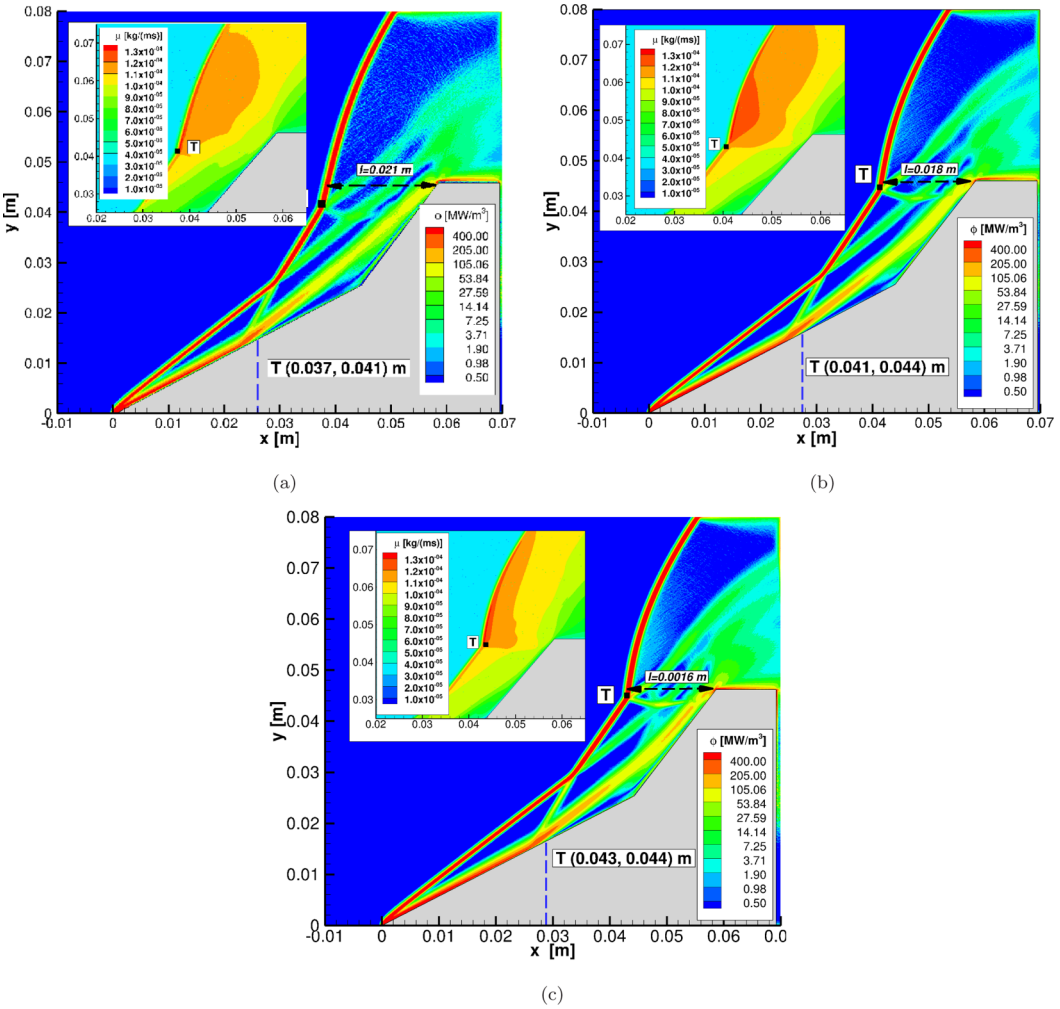

(a) (b) (c)

FIG. 18. Spatial distribution of viscous dissipation, (ϕ), at steady state and calculated based on $\phi = \mu[\nabla \boldsymbol{u} + (\nabla \boldsymbol{u})^{\dagger} - \frac{2}{3}\nabla \cdot \boldsymbol{u}\mathbf{l}] : \nabla \boldsymbol{u}$, where $\mathbf{l}$ is the identity matrix, $\boldsymbol{u}$ is the velocity field, and μ is dynamic viscosity shown in the insets. Note that the blue dashed vertical line shows the starting x location of the separation region. (a) Nitrogen case, (b) Non-reacting air case, and (c) Reacting air case.

and reacting air cases using the WPOD method and the residuals algorithm, based on the fact nonreacting and reacting air cases were simulated until 1.275 and 2.01 ms and the required computation hours are presented in Table VI.

V. SUMMARY AND CONCLUSIONS

The impact of thermochemical nonequilibrium effects on the time-dependent characteristics of hypersonic separated flows over a double wedge were investigated using high-fidelity, time-accurate DSMC coupled with the WPOD and residuals algorithm approaches. Edney type IV flow over a double-wedge geometry for pure nitrogen, a nonreacting nitrogen and oxygen mixture, and reacting air were considered and the WPOD method was applied to unsteady DSMC data for the first time. In contrast to similar previous work for nitrogen flows over a double cone, the presence of multiple chemical species and chemical reactions was observed to generate sinusoidal fluctuations

TABLE VI. DSMC numerical parameters for the simulations.

Numerical parameters[a]	Nitrogen	Nonreacting air	Reacting air
Number of simulated particles	1.45×10^9	1.288×10^9	1.258×10^9
Total number of time steps[b]	350 000	420 000	670 000
Total number of collision cells	90.5×10^6	41.4×10^6	26.65×10^6
Total computation hours[c] (CPU hours)	59,700	75,600	115,200

[a]At the end of the simulation.
[b]A time step of 3 ns is used for all cases.
[c]ERDC Topaz High Performance Computing System with 960 processors.

that asymptotically decay in the vicinity of the triple point. The WPOD method was applied to the DSMC time snapshots in order to decompose time-dependent flow-field parameters into spatiotemporal modes, to establish steady-state solutions, and reduce statistical noise.

The use of WPOD coupled with DSMC allowed us to understand a number of important trends. For all three cases, it was found that the spatial part of the first mode for each flow macroparameter is a good predictor of the corresponding steady-state solution since the magnitude of the first temporal mode is at least an order of magnitude higher compared to higher modes. Higher spatial POD modes, on the other hand, were observed to be larger in magnitude in the bow, separation and transmitted shocks, and shear layers, showing that these structures are strongly coupled. Because the temporal components of the POD modes for different flow-field quantities were found to have the same decay rates and circular frequencies, it was possible to correlate the orthogonal POD modes with global modes since the former were calculated when the flow was close to convergence. The temporal POD modes for the nonreacting and reacting air cases were shown to have the form of two-dimensional traveling waves not just in the vicinity of the triple point, but throughout the flow, allowing us to obtain the real and imaginary parts of the least damped eigenmode.

It was observed that the time behavior of the nitrogen and nonreacting and reacting air cases are different due to a complex interaction between the shock-shock interaction structures and flow-field translational temperatures for the same free stream conditions. In particular, the DSMC-WPOD analyses showed that the overall shock structure and the required time to reach steady state can change due to on the presence of multiple chemical species and chemical reactions. The shock standoff distance decreases from the nitrogen to the reacting air case, consistent with experiments. The region of the highest translational temperatures also decreases among the three cases since the modeling of endothermic reactions such as oxygen dissociation and $N_2 + O$ exchange reactions removes energy from the flow. In turn, larger regions of high temperatures associated with the shock-shock interaction region increases viscosity, which has a stabilizing effect on the flow, reducing the time to reach steady state even though the recirculation region is larger. The combination of these factors has the net effect of increasing the time required for the chemically reacting air case to reach steady state compared to pure nitrogen by approximately a factor of 2.

Finally, the steady-state solutions were predicted with a computational savings of about 45 000 CPU hours compared to the 160 000 that would have been required if the DSMC were used to compute the flow until steady state. Statistical fluctuations inherent to the DSMC method were reduced significantly by the use of the WPOD method, enabling us to predict the spatial distributions of trace species concentrations of NO as well as their vibrational temperatures.

ACKNOWLEDGMENTS

The research of O.T. and D.A.L. is being supported by the Air Force Office of Scientific Research through AFOSR Grant No. FA9550-11-1-0129 with a subcontract Award No. 2010-06171-01 to UIUC. O.T. and D.A.L. are also grateful for the computational resources provided on ERDC Topaz and Onyx, AFRL Thunder, and ARL Centennial. The work of V.T. is sponsored by the Air Force

Office of Scientific Research, Air Force Material Command, USAF, under Grant No. FA9550-15-1-0387, Global Transient Growth Mechanisms in High-Speed Flows with Application to the Elliptic Cone, and Grant No. FA9550-17-1-0115, Global Modal and Non-modal Instability Analyses of Shock-Induced Separation Bubbles.

APPENDIX A: DSMC METHOD, MODELS, AND NUMERICAL PARAMETERS

The DSMC method provides high-fidelity molecular transport and thermal nonequilibrium, commonly seen in strong shock-shock interactions, and inherently captures rarefaction effects such as velocity slip and temperature jump without an *a priori* specific model. The numerical analyses were performed using the Statistical Modeling in Low-Density Environment (SMILE) [40] solver. The variable hard sphere (VHS) [18] model was used in SMILE and the VHS cross section was modeled as

$$\sigma_{\mathrm{VHS}} = \frac{\pi d_{\mathrm{ref}}^2}{\Gamma(2.5-\omega)}\left[\frac{2T_{\mathrm{ref}}k}{(m_r g^2)}\right]^{(\omega-0.5)}, \tag{A1}$$

where k is the Boltzmann constant, g is the relative speed, m_r is the reduced mass, and Γ is the Γ function. The viscosity indexes, ω, and the collision diameters, d_{ref}, of each species at a reference temperature of 1000 K are presented in Table II. The Larsen-Borgnakke (LB) [41] model was employed to model rotational-translational (R-T) and vibrational-translational (V-T) energy transfer. In particular, Millikan and White (MW) [42] and Parker's rates [43] with the DSMC correction factors [44,45] were used to model V-T and R-T relaxation rates, respectively. According to the Parker model, the rotational collision number, which determines the probability of rotational inelastic collision (i.e., $\Pr = \frac{1}{Z_r}$) is given by

$$Z_r(T) = \frac{\zeta_t}{\zeta_t+\zeta_r}\frac{Z_{r,\infty}}{1+\frac{\pi^{3/2}}{2}\left(\frac{T^*}{T}\right)^{1/2}+\left(\frac{\pi^2}{4}+\pi\right)\frac{T^*}{T}}, \tag{A2}$$

where $Z_{r,\infty}$ and T^* are species specific and are given in Table II. Similarly, the vibrational relaxation number is expressed as

$$Z_v(T) = \frac{\zeta_t+\zeta_r}{\zeta_t+\zeta_r+\zeta_v}\frac{\exp\left(1.16\times10^{-3}m_r^{1/2}\theta^{4/3}\left(T^{-1/3}-0.015m_r^{1/4}\right)-18.42\right)/P+\tau_P}{\tau_c}, \tag{A3}$$

where ζ_t, ζ_r, and ζ_v are the translational, rotational, and vibrational degrees of freedom, respectively. Note that τ_c and τ_P are the mean collision time and the high-temperature correction suggested by Park [46], P is the pressure in atmospheres, and θ is the vibrational characteristic temperature for each species. A summary of these variables for the species used in this work is given in Table II.

The total collision energy (TCE) approach [18] was employed to model the aforementioned reactions given in Eqs. (1) and (2). The reaction rate, k, presented in the Arrhenius form is given in the following relationship,

$$k(T) = AT^B\exp(-E_a/kT), \tag{A4}$$

where A is the pre-exponential factor, B stands for the temperature dependence, and E_d is the activation energy. The values for the dissociation and exchange reactions are given in Table VII and are taken from Ref. [47].

TABLE VII. Rate coefficient parameters.

Reaction	A [m^3 s^{-1}]	B	E_a, [J]
Eq. (1)	3.32×10^{-9}	-1.50	8.214×10^{-19}
Eq. (2)	9.45×10^{-18}	0.42	5.928×10^{-19}

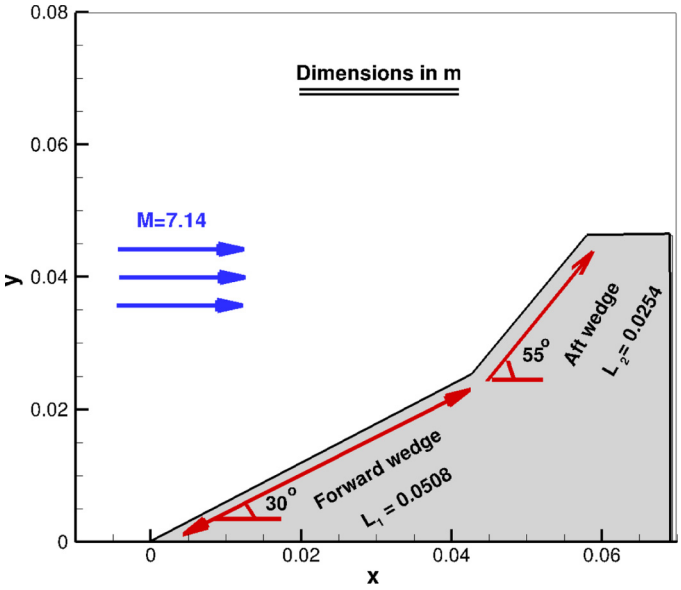

FIG. 19. Double-wedge configuration and size of the simulation domain.

Since the strong shock interactions and flow separation results in a wide, local Knudsen number range, the numerical parameters of DSMC were correctly selected to model molecular interactions and chemical reactions. As presented in Table VI, more than 1 billion computational particles are used for the 2-D simulations to provide a sufficient number of particles for background and collision cells. As discussed in the details given in Ref. [10], SMILE uses a two-level Cartesian mesh, particularly the background (coarser) and the collision (finer) grids. In this work, 800×800 evenly distributed background cells in the x and y directions are used to capture large flow gradients in the flow-field parameters (see Fig. 19 for details regarding the simulation domain and geometry). It should be noted that the sampling of macroparameters takes place in the background cells and the background grid provides sufficient statistics to sample the macroparameters during a single time step. The refined collision grid is constructed by subdividing the background grid and in the current work, the maximum number of subdivisions in a background cell is 30×30 in the x and y directions. As will be discussed next, this number of subdivided cells, or collision cells, is sufficient to calculate the majorant collision frequency [48] accurately. Since the free-stream number density is the same for all cases, the reacting air case, the most challenging one, in terms of DSMC numerical parameters is discussed in detail.

Figure 20 shows the spatial distribution of the DSMC numerical parameters for the reacting air case. As shown in Fig. 20(a), the collision cell size is sufficiently small such that the ratio of the local mean free path to the length of collision cells (i.e., $\lambda/\Delta x$) is larger than unity throughout the domain. In particular, the minimum value of 1.2 in the separation region meets the DSMC criterion for shock-dominated flows [32]. Similarly, a time step of 3×10^{-9} s was chosen such that the ratio of the mean collision time to the time step is greater than the unity throughout the domain, as shown in Fig. 20(b). Note that although the time step and collision cell size meet the DSMC criteria, the dependence of surface parameters on these criteria was further tested by decreasing the collision cell size by a factor of about 1.4 (i.e., finer case) and by increasing the time step by a factor of 0.75 for the reacting air case. As can be seen in Fig. 3(b), the heat fluxes close to steady-state are found to be essentially the same, showing that the most challenging reacting air case is independent of any DSMC numerical parameters. Figure 20(c) shows that the number of particles in collision cells inside the shock region is about 40, providing about four computational particles per collision

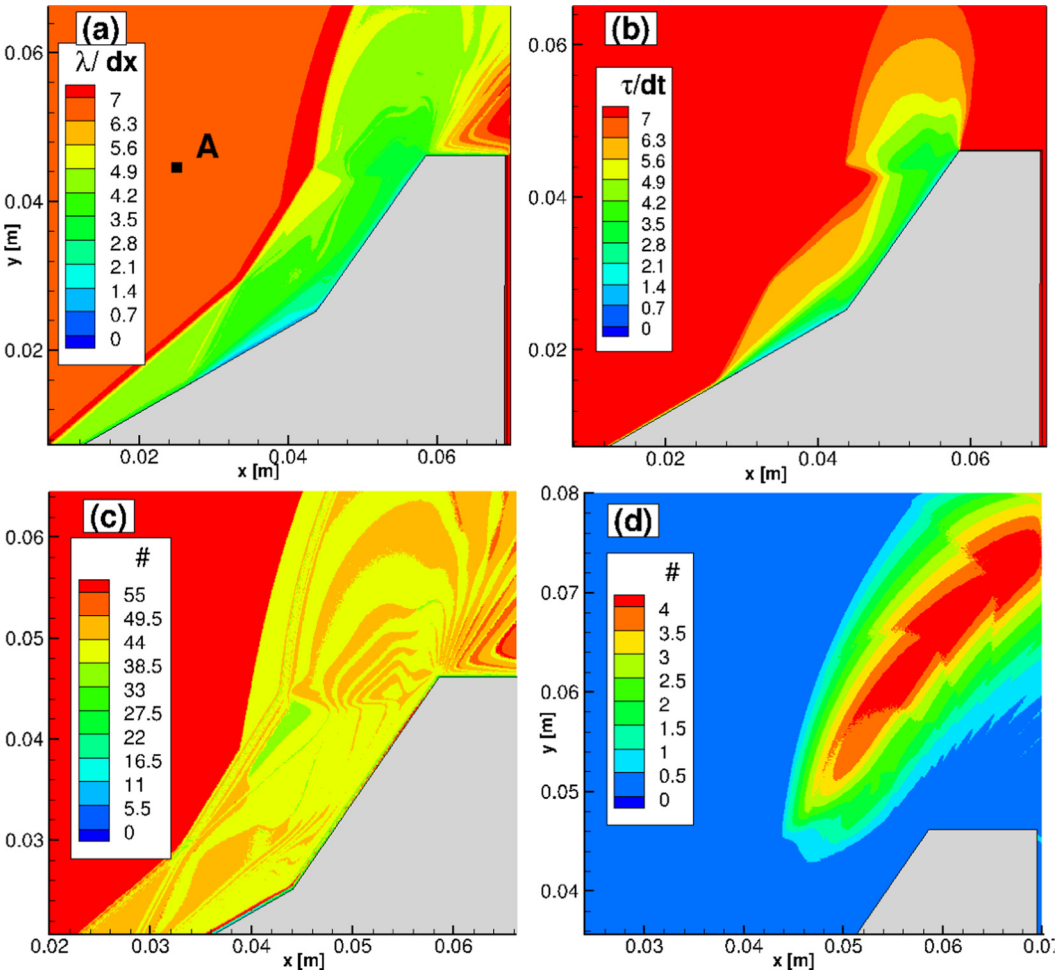

FIG. 20. Spatial distribution of numerical parameters for the reacting air case at 2 ms: (a) ratio of local mean free path to the length of the collision cells, (b) mean collision time normalized by the time step, (c) number of particles for all species in collision cell, and (d) number of O particles in collision cell.

cell for the trace species of atomic oxygen, as can be seen in Fig. 20(d). This number of particles is sufficient for the majorant collision algorithm [48] to model the exchange reaction accurately. Relatively fewer particles per collision cell downstream of the shocks were used in the nitrogen and nonreacting air cases (not shown) with respective values of 15 and 30 since chemical reactions were not modeled for these cases. The amount of statistical fluctuations in a background cell are also comparable since the resolution of the background cell is the same for all cases. In particular, the standard deviations of the x velocity and translation temperature fields for the background cell located at A [see Fig. 20(a)] are 14.62 ms^{-1} and 18.53 K with mean values of 3810.7 ms^{-1} and 713.95 K, respectively. Note that the average number of particles over time at this location is about 1003. Since the total number of particles is large, the amount of statistical noise for the translational temperature field is about 2.6% of the mean.

APPENDIX B: NUMERICAL CONVERGENCE OF WPOD PARAMETERS

The percentage differences between the WPOD and DSMC solution for the nitrogen case were examined and it was found that there is a maximum percentage difference of less than 3% in the

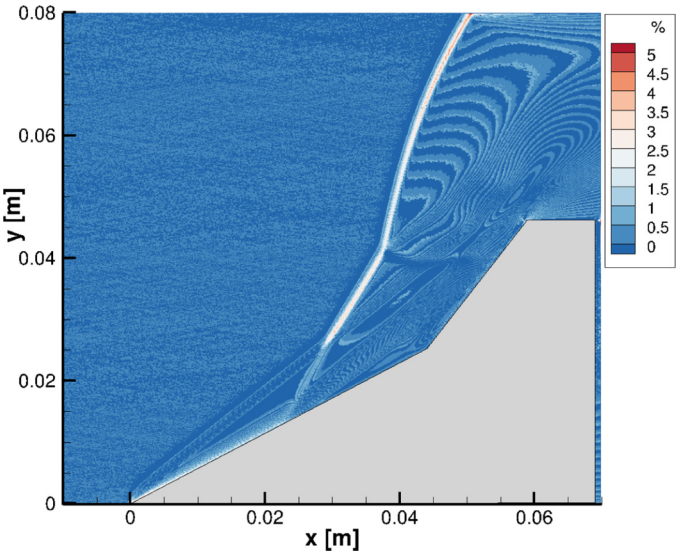

FIG. 21. Percentage differences between the WPOD and DSMC solutions for the y-velocity field, calculated as $\% = (v(\mathrm{x},\mathrm{y})_{\mathrm{POD}} - v(\mathrm{x},\mathrm{y})_{\mathrm{DSMC}})/u_\infty \times 100$.

bow shock region, as can be seen in Fig. 21. This small discrepancy can be attributed to the fact that the second POD mode is still somewhat active at 1.05 ms, as shown by the second mode of Fig. 5, but it is also possible that 500 time-step samples are insufficient to reduce the DSMC statistical fluctuations to be less than 3% in this region.

To verify that the previously estimated damping rates are independent of the number of snapshots used in the baseline case, the number of WPOD snapshots is increased by a factor of 2 and is designated as "2X Resolution" in Fig. 22(a), where a comparison of the two primary temporal modes of the rotational temperatures is shown. Perfect agreement is achieved between these two cases, demonstrating that the previously shown temporal parts are independent of the number of

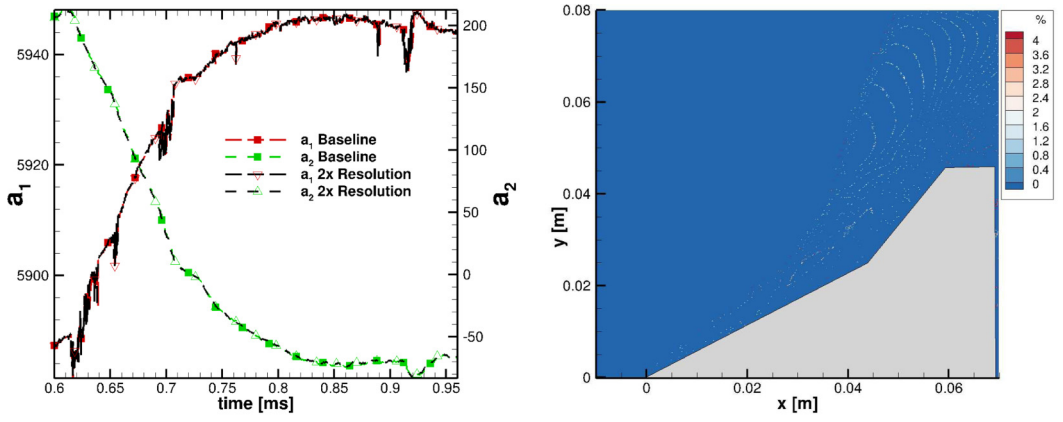

(a) (b)

FIG. 22. Convergence of the WPOD time windows for the rotational temperatures of nitrogen molecules. (a) Comparison of temporal modes and (b) Percentage differences.

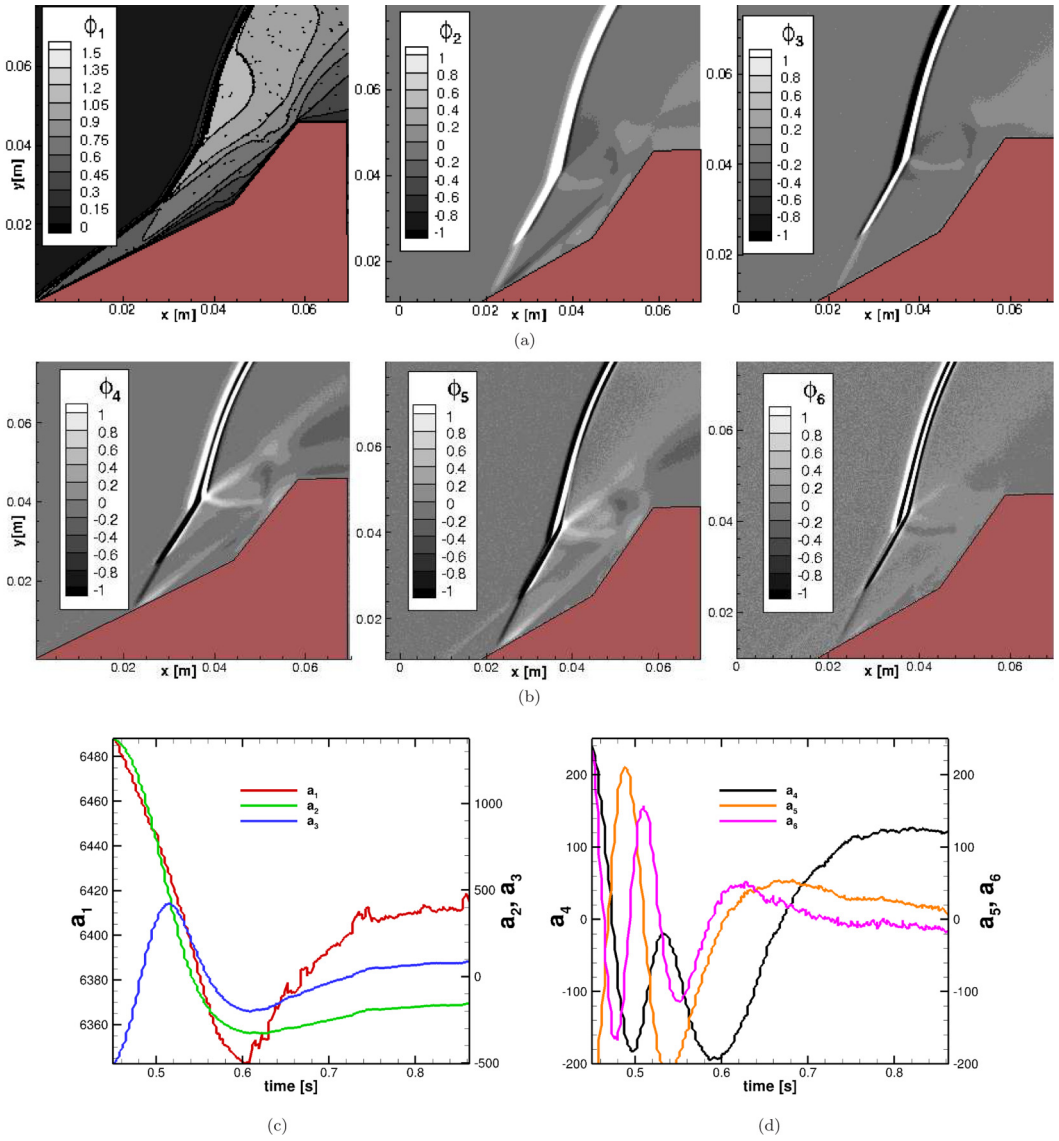

FIG. 23. POD modes for the translational temperature of nitrogen molecules calculated between 0.45 and 0.861 ms based on 275 snapshots. (a) Spatial first three modes, (b) Spatial 4th, 5th, and 6th modes, (c) Temporal first three modes, and (d) Temporal 4th, 5th, and 6th modes.

snapshots used. Similarly, percentage differences between these two cases for the first spatial mode of the rotational temperatures are shown in Fig. 22(b), where the maximum difference is found to be less than 2%. Therefore, the number of time windows is sufficient to capture the spatial variation and time evolution of the nitrogen flow. It should be noted that the small striations seen in Fig. 22(b) as well as in Fig. 8(b) can be attributed to the variations of the number of particles in the background cells.

Figure 23 shows the spatial and temporal parts of six POD modes for the translational temperatures of the nitrogen case calculated between 0.45 and 0.861 ms, providing an opportunity to investigate the time dependency of the POD modes when an earlier time interval is used. A

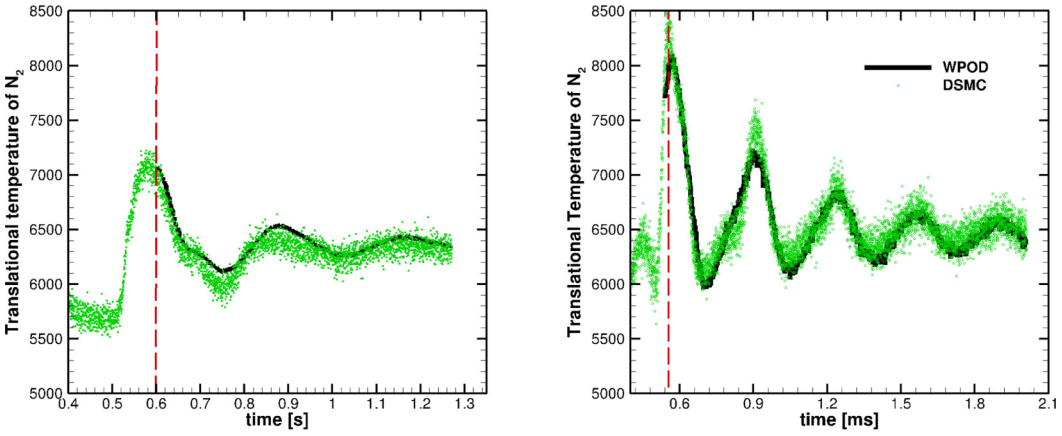

(a) (b)

FIG. 24. Comparison of translational temperatures at location 1 shown in Fig. 1 for the WPOD and DSMC methods. (a) Non-reacting air case and (b) Reacting air case.

comparison of the first mode of the translational temperatures of Fig. 23(a) with Fig. 6 shows that the spatial distribution is found to be essentially the same since the first mode outlines the steady-state solution. As opposed to the baseline case where the WPOD method was applied between 0.6 and 0.96 ms, the number of modes required to accurately represent the flow-field parameters is now equal to six, in contrast to the value of three for the baseline case. Overall, most of the variations are found to be prominent in the bow shock and shear layers. It should also be noted that the third mode of the baseline case shows a remarkable resemblance to the fifth mode of the current case since these modes correspond to the least damped eigenmodes of global modes.

Lastly, the accuracy of the previously presented POD modes is tested by comparing the DSMC probed data at location 1 shown in Fig. 1 with a solution constructed based on the POD modes using Eq. (7). It should be noted that the DSMC probe data are recorded at each time step, whereas the POD time window data are written every 500 time steps for nonreacting and reacting air cases. As shown in Fig. 24, the DSMC data in the vicinity of the triple point are found to be in good agreement with the POD solution, showing that the presented POD modes in this work were determined accurately and the number of time windows is sufficient to capture the time-dependent behavior. It can also be seen that the DSMC statistical fluctuations are significantly reduced.

[1] M. S. Holden and T. P. Wadhams, Code validation study of laminar shock/boundary layer and shock/shock interactions in hypersonic flow. Part A: Experimental measurements, AIAA Paper 2001-1031, 2001.

[2] M. S. Holden, T. P. Wadhams, J. K. Harvey, and G. V. Candler, Comparisons between DSMC and Navier-Stokes solutions on measurements in regions of laminar shock wave boundary layer interaction in hypersonic flows, AIAA Paper 2002-0435, 2002.

[3] H. Babinsky and J. K. Harvey, *Shock Wave-Boundary-Layer Interactions* (Cambridge University Press, Cambridge, UK, 2011).

[4] A. B. Swantek and J. M. Austin, Flowfield establishment in hypervelocity shock-wave/boundary-layer interactions, AIAA J. **53**, 311 (2014).

[5] D. Knight, O. Chazot, J. Austin, M. A. Badr, G. Candler, B. Celik, D. de Rosa, R. Donelli, J. Komives, A. Lani *et al.*, Assessment of predictive capabilities for aerodynamic heating in hypersonic flow, Progr. Aerospace Sci. **90**, 39 (2017).

[6] M. E. Erengil and D. S. Dolling, Unsteady wave structure near separation in a Mach 5 compression ramp interaction, AIAA J. **29**, 728 (1991).
[7] J. P. Dussauge, P. Dupont, and J. F. Debiève, Unsteadiness in shock wave boundary layer interactions with separation, Aerosp. Sci. Technol. **10**, 85 (2006).
[8] M. Wu and M. P. Martin, Analysis of shock motion in shockwave and turbulent boundary layer interaction using direct numerical simulation data, J. Fluid Mech. **594**, 71 (2008).
[9] L. Vanstone, D. Estruch-Samper, and B. Ganapathisubramani, Establishment times of hypersonic shock-wave/boundary-layer interactions in intermittent facilities, AIAA J. **55**, 2875 (2017).
[10] O. Tumuklu, D. A Levin, and V. Theofilis, Investigation of unsteady, hypersonic, laminar separated flows over a double cone geometry using a kinetic approach, Phys. Fluids **30**, 046103 (2018).
[11] V. Theofilis, On steady–state flow solutions and their nonparallel global linear instability, in *Proceedings of the 8th European Turbulence Conference*, edited by C. Dopazo (International Center for Numerical Methods in Engineering, Barcelona, Spain, 2000), pp. 35–38.
[12] O. Tumuklu, D. A Levin, and V. Theofilis, Numerical study of temporal characteristics of highly expanded hypersonic flows over a tick geometry (unpublished).
[13] B. E. Edney, Effects of shock impingement on the heat transfer around blunt bodies, AIAA J. **6**, 15 (1968).
[14] S. R. Sanderson, H. G. Hornung, and B. Sturtevant, The influence of non-equilibrium dissociation on the flow produced by shock impingement on a blunt body, J. Fluid Mech. **516**, 1 (2004).
[15] G. H. Furumoto, X. Zhong, and J. C. Skiba, Numerical studies of real-gas effects on two-dimensional hypersonic shock-wave/boundary-layer interaction, Phys. Fluids **9**, 191 (1997).
[16] A. Grumet, J. Anderson, Jr., and M. Lewis, A numerical study of shock wave/boundary layer interaction in nonequilibrium chemically reacting air: The effects of catalytic walls, in *Proceedings of the 29th Aerospace Sciences Meeting* (AIAA, Reston, VA, 1991), AIAA-Paper 91-0245.
[17] M. R. Malik and E. C. Anderson, Real gas effects on hypersonic boundary-layer stability, Phys. Fluids A: Fluid Dyn. **3**, 803 (1991).
[18] G. A. Bird, *Molecular Gas Dynamics and the Direct Simulation of Gas Flows* (Clarendon Press, Oxford, UK, 1994).
[19] J. L. Lumley, The structure of inhomogeneous turbulent flows: Atmospheric turbulence and radio wave propagation (unpublished).
[20] See Supplemental Material at http://link.aps.org/supplemental/10.1103/PhysRevFluids.4.033403 for containing three movies showing the time evolution of the flow field parameters.
[21] P. J. Schmid, Dynamic mode decomposition of numerical and experimental data, J. Fluid Mech. **656**, 5 (2010).
[22] J. N. Kutz, S. L. Brunton, B. W. Brunton, and J. L. Proctor, *Dynamic Mode Decomposition: Data-Driven Modeling of Complex Systems* (SIAM, Philadelphia, 2016), Vol. 149.
[23] K. Taira, S. L. Brunton, S. T. M. Dawson, C. W. Rowley, T. Colonius, B. J. McKeon, O. T. Schmidt, S. Gordeyev, V. Theofilis, and L. S. Ukeiley, Modal analysis of fluid flows: An overview, AIAA J. **55**, 4013 (2017).
[24] B. R. Noack, From snapshots to modal expansions: Bridging low residuals and pure frequencies, J. Fluid Mech. **802**, 1 (2016).
[25] P. Holmes, J. L. Lumley, G. Berkooz, and C. W. Rowley, *Turbulence, Coherent Structures, Dynamical systems, and Symmetry* (Cambridge University Press, Cambridge, UK, 2012).
[26] D. M. Luchtenburg, B. R. Noack, and M. Schlegel, An introduction to the POD galerkin method for fluid flows with analytical examples and matlab source codes, Technical Report 01/2009, Berlin Institute of Technology, Berlin, Germany, 2009.
[27] L. Grinberg, Proper orthogonal decomposition of atomistic flow simulations, J. Comput. Phys. **231**, 5542 (2012).
[28] V. Theofilis and T. Colonius, An algorithm for the recovery of 2- and 3D biglobal instabilities of compressible flow over 2D open cavities, in *Proceedings of the 33rd AIAA Fluid Dynamics Conference and Exhibit, Fluid Dynamics and Co-located Conferences* (AIAA, Reston, VA, 2003), AIAA-Paper 2003-4143.

[29] O. Tumuklu, D. A. Levin, and J. M. Austin, Shock-shock interactions for a double wedge configuration in different gases, in *Proceedings of the 53rd AIAA Aerospace Sciences Meeting, AIAA SciTech Forum* (AIAA, Reston, VA, 2015), AIAA-Paper 2015-1520.

[30] O. Tumuklu, D. A. Levin, S. F. Gimelshein, and J. M. Austin, Modeling of near-continuum laminar boundary layer shocks using DSMC, in *Proceedings of the Thirtieth International Symposium on Rarefied Gas Dynamics: RGD30*, edited by A. Ketsdever and H. Struchtrup, AIP Conf. Proc. Vol. 1786 (AIP Publishing, Melville, NY, 2016), p. 050004.

[31] S. S. Sawant, O. Tumuklu, R. Jambunathan, and D. A Levin, Application of adaptively refined unstructured grids in dsmc to shock wave simulations, Comput. Fluids **170**, 197 (2018).

[32] J. N. Moss and G. A. Bird, Direct simulation Monte Carlo of hypersonic flows with shock interactions, AIAA J. **43**, 2565 (2005).

[33] O. Tumuklu, V. Theofilis, and D. A. Levin, On the unsteadiness of shock–laminar boundary layer interactions of hypersonic flows over a double cone, Phys. Fluids **30**, 106111 (2018).

[34] O. Tumuklu, D. A. Levin, and V. Theofilis, On the temporal evolution in laminar separated boundary layer shock-interaction flows using DSMC, in *Proceedings of the 55th AIAA Aerospace Sciences Meeting, AIAA SciTech Forum* (AIAA, Reston, VA, 2017), AIAA-Paper 2017-1614.

[35] L. Sirovich, Turbulence and the dynamics of coherent structures, Q. Appl. Math. **45**, 561 (1987).

[36] O. Tumuklu, Modeling of shock boundary layer interactions and stability analysis using particle approaches, Ph.D. thesis, University of Illinois at Urbana-Champaign, 2018.

[37] R. Kumar, A. K. Chinnappan, and M. V. Akhil, Denoising of direct simulation Monte Carlo data using proper orthogonal decomposition technique, J. Spacecr. Rockets **55**, 841 (2018).

[38] V. Theofilis, Global linear instability, Annu. Rev. Fluid Mech. **43**, 319 (2011).

[39] A. Manela and J. Zhang, The effect of compressibility on the stability of wall-bounded Kolmogorov flow, J. Fluid Mech. **694**, 29 (2012).

[40] M. S. Ivanov, G. N. Markelov, and S. G. Gimelshein, Statistical simulation of reactive rarefied flows: Numerical approach and applications, in *Proceedings of the 7th AIAA/ASME Joint Thermophysics and Heat Transfer Conference* (AIAA, Reston, VA, 1998), AIAA-Paper 1998-2669.

[41] P. S. Larsen and C. Borgnakke, Statistical collision model for Monte Carlo simulation of polyatomic gas mixture, J. Comput. Phys. **18**, 405 (1975).

[42] R. C. Millikan and D. R. White, Systematics of vibrational relaxation, J. Chem. Phys. **39**, 3209 (1963).

[43] J. G. Parker, Rotational and vibrational relaxation in diatomic gases, Phys. Fluids **2**, 449 (1959).

[44] F. E. Lumpkin, B. L. Haas, and I. D. Boyd, Resolution of differences between collision number definitions in particle and continuum simulations, Phys. Fluids A: Fluid Dyn. **3**, 2282 (1991).

[45] N. E. Gimelshein, S. F. Gimelshein, and D. A. Levin, Vibrational relaxation rates in the direct simulation Monte Carlo method, Phys. Fluids **14**, 4452 (2002).

[46] C. Park, Problems of rate chemistry in the flight regimes of aeroassisted orbital transfer vehicles, Prog. Astronaut. Aeronaut. **96**, 511 (1985).

[47] T. Ozawa, J. Zhong, and D. A. Levin, Development of kinetic-based energy exchange models for noncontinuum, ionized hypersonic flows, Phys. Fluids **20**, 046102 (2008).

[48] M. S. Ivanov and S. V. Rogasinsky, Analysis of the numerical techniques of the direct simulation Monte Carlo method in the rarefied gas dynamics, Soviet J. Num. Anal. Math. Model. **3**, 453 (1988).